

Universität Bonn

Physikalisches Institut

Studies of Tau-Lepton Polarisation in Decays of Higgs and Z Bosons with the ATLAS Experiment

Michaela Roggendorf

The Tau-Lepton Polarisation is studied in Decays of 125 GeV Higgs and Z Bosons with regard to the separation power. Three different observables: the fraction of visible energy x , the charged energy asymmetry Υ and the polarimetric vector h are discussed in this study.

The analysis is based on Monte Carlo simulated proton-proton collisions at 8 TeV center-of-mass energy at LHC, collected by the ATLAS detector. Each variable is evaluated regarding the theoretical and observed separation power between tau leptons with positive and negative helicity, followed by the separation power between 125 GeV Higgs and Z Bosons.

Physikalisches Institut der
Universität Bonn
Nussallee 12
D-53115 Bonn



BONN-IB-2014-03
Januar 2014

Universität Bonn

Physikalisches Institut

Studies of Tau-Lepton Polarisation in Decays of Higgs and Z Bosons with the ATLAS Experiment

Michaela Roggendorf

Dieser Forschungsbericht wurde als Masterarbeit von der Mathematisch-Naturwissenschaftlichen Fakultät der Universität Bonn angenommen.

Angenommen am: 31.10.2013
1. Gutachter: Prof. Dr. Nobert Wermes
2. Gutachter: Prof. Dr. Ian C. Brock

Acknowledgements

I would like to thank Prof. Norbert Wermes for providing me the opportunity of being part of his research group, supporting me with a lot of helpful information and being referee for this thesis. I would also like to thank Prof. Dr. Ian C. Brock for being the second referee for my final examination.

I would like to express my appreciation to my supervisor, Dr. Jürgen Kroseberg. This thesis would not have been possible without his help, support, patience and engagement.

I am particularly grateful for the help introducing me to the topic as well for the advice and support on the way, given by Thomas Schwindt. I am deeply grateful to Benedict Winter for providing me with samples for my analysis and helping me with the implementation into my studies. Moreover, I would like to thank all members in our group for the useful comments, remarks and discussion through the time of this thesis helping me putting pieces together.

Finally, I would like to thank my parents and my boyfriend, who have supported me throughout the entire process.

Contents

1	Introduction	1
2	The Standard Model of Particle Physics	3
2.1	The Electroweak Standard Model	4
2.2	Quantum Chromo Dynamics (QCD)	5
2.3	Higgs Mechanism	6
2.4	Running Coupling	8
2.5	Limitations of the Standard Model	8
3	The ATLAS Experiment	9
3.1	ATLAS Coordinate System	10
3.2	Particle Detection in ATLAS	10
3.2.1	Major Detector Components	10
3.2.2	Trigger and Data Storage	11
3.3	Particle Identification	12
3.3.1	Electrons	12
3.3.2	Muons	13
3.3.3	Jets	13
3.3.4	Missing Transverse Energy (MET)	13
3.3.5	Tau Leptons	14
3.3.6	Overlap Removal	14
3.4	Event Generation and Detector Simulation	14
3.4.1	Hard Scattering and Underlying Event	14
3.4.2	Proton-Proton Scattering Process	15
3.4.3	Event Generators and Detector Simulation	16
4	Higgs and Z Boson at Hadron Colliders	17
4.1	Z Boson at Hadron Colliders	18
4.2	Higgs Boson at Hadron Colliders	18
4.3	Higgs and Z boson distinction and polarisation information	20
5	Tau-Lepton Spin Information	23
5.1	Tau Decays	23
5.2	Polarisation Information in Simulated Events	24
5.2.1	TauSpinner	24

5.3	Reconstruction of Tau Decay Products	26
5.3.1	Neutral Pion Reconstruction	26
5.3.2	Neutrino Reconstruction	27
5.4	Polarisation Observables in Tau Decays	29
5.4.1	Fraction of Visible Energy	29
5.4.2	Charged Energy Asymmetry	33
5.4.3	Spin and Polarimetric Vectors	34
6	Analysis	35
6.1	Event Selection	35
6.2	Performance Evaluation	36
6.2.1	Single Tau Lepton Analysis	36
6.2.2	Di-Tau Analysis	37
6.3	Tau Lepton Helicity Reconstruction	39
6.3.1	Fraction of Visible Energy	39
6.3.2	Charged Energy Asymmetry	42
6.3.3	Polarimetric Vectors	43
6.3.4	Conclusions	47
6.4	Polarisation of H/Z in Monte Carlo Samples	48
6.4.1	Distinction using Truth Information	48
6.4.2	Distinction after Reconstruction	51
6.4.3	Combined Analysis in the $\rho\rho$ -Channel	53
6.4.4	Conclusions	54
7	Conclusions and Outlook	55
A	Useful information	57
A.1	Detector Acceptance in pseudorapidity	57
A.2	Charged Energy Asymmetry Reconstruction with Channel Match	58
A.3	Additional Observable Correlations	59
A.4	TMVA analysis in the $\rho\rho$ -channel	60

Introduction

In high-energy particle physics the main aim is to understand how matter is built from fundamental particles, what their characteristics are and how they interact with each other. The smaller the objects are the more energy is needed to create and the more effort is needed to later observe these objects. Therefore large particle colliders and also detectors were built. The currently highest-energy collider in terms of center-of-mass energy as well as beam energy is the ring accelerator called Large Hadron Collider (LHC), which was first started on 10 September 2008. One of the two big general purpose detectors at the LHC is the ATLAS detector. The Higgs boson is the last missing particle of the Standard Model of Particle Physics and its existence was predicted 1964 as a consequence of the Higgs mechanism [1], which was needed to give masses to the particles of the Standard Model. In 2012, after a search of almost 50 years a new neutral boson, compatible with a Standard Model Higgs boson, with a mass of about 125 GeV was observed in the ATLAS [2] and the CMS experiment [3]. The observation of the new particle is only the first step, now it has to be verified that the newly discovered particle really is the Standard Model Higgs boson sought for by testing all its predicted properties.

A particularly interesting Higgs decay channel is the decay into a pair of tau leptons since this is the leptonic decay channel with a large fraction. Since only a weak evidence [4] could yet be found in this channel and the long shut down of the LHC has started, meaning that the amount of data is unchanged until the new start planned for 2015, it becomes more and more important to improve the analysis of the present data. A very important part in the Higgs search is to provide an efficient separation of possible Higgs candidates and background processes. The major background in the $H \rightarrow \tau\tau$ analysis is coming from Z bosons decaying into tau lepton pairs and, therefore results in the same final state with an invariant mass close to the mass region of the signal. A promising criterion to suppress this background is the spin, since the Higgs boson is a spin-zero and the Z boson a spin-one particle. This spin has a measureable effect the polarisation of the daughter particles. In this thesis, the tau lepton polarisation in decays of Higgs and Z bosons is studied in view of a possible Higgs/ Z separation.

The Standard Model of Particle Physics

The Standard Model of particle physics is a theory that includes all up to now observed elementary particles (shown in 2.1) and their interactions except for gravitation. The particles are divided into two classes: the twelve particles which form matter and have a half-integer spin named fermions and the five mediators with an integer spin named bosons. Fermions can also be divided into two smaller groups: the leptons, which take part in the weak interaction mediated by the Z and the W boson and the quarks which can additionally interact via the strong force mediated by the gluon. All charged particles take part in the electromagnetic interaction mediated by the photon.

	I	II	III		
mass	2.3MeV	1.275GeV	173.07GeV	0MeV	126GeV?
charge	2/3	2/3	2/3	0	0
spin	1/2	1/2	1/2	1	0
Q	<i>u</i>	<i>c</i>	<i>t</i>	<i>g</i>	<i>H</i>
U	up	charm	top	gluon	Higgs boson
A	4.8MeV	95MeV	4.18GeV	0MeV	
R	-1/3	-1/3	-1/3	0	
K	1/2	1/2	1/2	1	
S	<i>d</i>	<i>s</i>	<i>b</i>	γ	
	down	strange	top	photon	
L	0.511MeV	105.7MeV	1.77GeV	91.2GeV	
E	-1	-1	-1	0	
P	1/2	1/2	1/2	1	
	<i>e</i>	μ	τ	<i>Z</i>	
	electron	muon	tau	Z boson	
T	<2eV	<2eV	<2eV	80.4GeV	
O	0	0	0	+/-1	
N	1/2	1/2	1/2	1	
S	ν_e	ν_μ	ν_τ	<i>W</i> $^\pm$	
	electron neutrino	muon neutrino	tau neutrino	W boson	

Figure 2.1: Particles of the Standard Model (values from [5])

The mathematical concept to describe all these particles and their interactions including relativistic and quantum mechanical effects, is a quantum field theory (QFT) based on the $SU(3)_{\text{colour}} \otimes SU(2)_{\text{weak}} \otimes U(1)_{\text{hyper}}$ symmetry group. In the following a short summary of some parts relevant for this thesis is given, more detailed information can be found in [6]. QFT unifies particles and fields including quantum mechanics and classical field theories, with the result that a particle can

be regarded as the excitation of the quantum field. It is required that the theory is invariant under local gauge transformations.

2.1 The Electroweak Standard Model

The weak interaction quantity comparable to electric charge in the electromagnetic interaction is called weak isospin T . The description of weak interactions and electromagnetic interaction can be combined such that the expression is independent under $SU(2)_T \times U(1)_Y$ transformations, because the isospin and the electromagnetic charge are related in the following way:

$$Q = \frac{Y}{2} + T_3, \quad (2.1)$$

where Y is the weak hypercharge and T_3 the third component of the weak isospin.

A characteristic of weak interaction is that left- and right-handed particles are interacting differently. For example the W boson can only decay into left-handed particles, whereas the Z can decay into left- or right-handed particles but with different coupling strength. The projection of the spin \vec{s} onto the momentum of the particle \vec{p} is called helicity with the helicity operator

$$\hat{h} = \frac{\vec{s} \cdot \vec{p}}{|\vec{p}|} = \frac{1}{2} \frac{\vec{\sigma} \cdot \vec{p}}{|\vec{p}|} \quad (2.2)$$

with $\vec{\sigma}$ being the vector of the 2×2 Pauli spin matrices σ_i given above. Helicity is conserved in electromagnetic and strong interactions but not in weak interactions. Another problem of the definition of helicity is that it is not Lorentz-invariant for massive particles. While a massless particle is moving with the speed of light, massive particles are moving with less speed therefore it is possible to change to a reference frame in which the particle is moving in reverse direction changing the sign of helicity. A closely related but Lorentz-invariant quantity is chirality. The chirality operator is γ^5 , therefore eigenstates of γ^5 (either +1 or -1) are defined as left- and right-handed chiral states. In the ultra-relativistic limit ($m \ll E$) chiral eigenstates correspond to helicity eigenstates. The projection operators for right-handed or respectively left-handed states are:

$$P_R = \frac{1}{2}(1 + \gamma^5) \quad P_L = \frac{1}{2}(1 - \gamma^5) \quad (2.3)$$

with $\gamma^5 = i\gamma^0\gamma^1\gamma^2\gamma^3$.

Regarding the weak isospin left-handed fermions form doublets and right-handed fermions singlets shown in Table 2.1. Right-handed neutrinos are not shown in the table because they have not been observed yet.

fermions	generation			Q/e	T_3
quarks	$\begin{pmatrix} u \\ d' \end{pmatrix}_L$	$\begin{pmatrix} c \\ s' \end{pmatrix}_L$	$\begin{pmatrix} t \\ b' \end{pmatrix}_L$	+2/3	+1/2
	u_R	c_R	t_R	-1/3	-1/2
	d_R	s_R	b_R	-2/3	0
				+1/3	0
leptons	$\begin{pmatrix} \nu_e \\ e \end{pmatrix}_L$	$\begin{pmatrix} \nu_\mu \\ \mu \end{pmatrix}_L$	$\begin{pmatrix} \nu_\tau \\ \tau \end{pmatrix}_L$	0	+1/2
	e_R	μ_R	τ_R	-1	-1/2
				+1	0

Table 2.1: Multiplet-structure of fermions in the Standard Model.

In consequence of the $SU(2)_T \times U(1)_Y$ transformation symmetry three fields W_μ^1 , W_μ^2 and W_μ^3 coupling to the weak isospin and a field B_μ coupling to the weak hypercharge are created. The Lagrange densities for these fields are

$$\mathcal{L}_{EW1} = -\frac{1}{4}W_{\mu\nu}^a W^{a,\mu\nu} - \frac{1}{4}B_{\mu\nu}B^{\mu\nu}, \quad (2.4)$$

where the field-strength tensors $W_{\mu\nu}^a$ and $B_{\mu\nu}$ can be expressed as

$$W_{\mu\nu}^a = \partial_\mu W_\nu^a - \partial_\nu W_\mu^a + g_W \varepsilon^{abc} W_\mu^b W_\nu^c \quad (2.5)$$

$$B_{\mu\nu} = \partial_\mu B_\nu - \partial_\nu B_\mu \quad (2.6)$$

with the Levi-Civita symbol ε^{abc} and the coupling strengths g_W and g'_W between weak isospin current and the boson fields B and W . It is not possible to include a mass term since this would destroy the gauge invariance needed for renormalisation. The same applies to the lagrangian related to the fermions, described by

$$\mathcal{L}_{EW2} = i\bar{\psi}_R \gamma^\mu D_\mu \psi_R + i\bar{\psi}_L \gamma^\mu D_\mu \psi_L \quad (2.7)$$

$$D_\mu \psi_R = [\partial_\mu + ig'_W B_\mu] \psi_R \quad (2.8)$$

$$D_\mu \psi_L = [\partial_\mu + \frac{i}{2}g'_W B_\mu - \frac{i}{2}g_W \sigma^i W_\mu^i] \psi_L. \quad (2.9)$$

2.2 Quantum Chromo Dynamics (QCD)

The strong interactions of colour carrying quarks and gluons are described in QCD, a $SU(3)$ transformation group. This colour concept is needed because neither quarks nor gluons are observed as free particles but grouped as colour-neutral combinations named hadrons, this effect is called colour confinement. Three different colour charges, red, green and blue, and the respective anti-colours are introduced. Each quark regardless of its flavour carries a colour charge while anti-quarks carry anti-colours and gluons are carrying a colour and a anti-colour at the same time. The fact that the gluons themselves carry colour leads to gluon self-interactions.

To preserve the local gauge invariance it is necessary to introduce eight massless gauge boson fields G_μ^a , where $a = 1, 2, \dots, 8$, which by means of the quark-fields q leads to the lagrangian

$$\mathcal{L}_{QCD} = -\frac{1}{4}G_{\mu\nu}^a G^{a,\mu\nu} - \bar{q}(i\gamma_\mu D^\mu)q. \quad (2.10)$$

The covariant derivative

$$D^\mu = \partial_\mu + ig_S(t^a G_\mu^a) \quad (2.11)$$

contains the coupling strength g_S of the gauge bosons, also called gluons, to the eight generators t^a and the field strength tensors $G_{\mu\nu}^a$ are given by

$$G_{\mu\nu}^a = \partial_\mu G_\nu^a - \partial_\nu G_\mu^a + g_S f^{abc} G_\mu^b G_\nu^c \quad (2.12)$$

with the structure constants f^{abc} ($a,b,c=1,2,\dots,8$) fulfilling the equation $[t^a, t^b] = i f^{abc} t^c$.

2.3 Higgs Mechanism

Symmetry Breaking

The problem up to this point is that all these theories only describe massless gauge bosons to preserve the gauge invariance, but the observed mediators of weak interaction do have mass. Therefore an indirect way to introduce masses in the model is needed that does not destroy the gauge invariance. This is done by spontaneous symmetry breaking via the Higgs mechanism, in which a complex scalar field $\Phi = \frac{1}{\sqrt{2}}(\Phi_1 + i\Phi_2)$ (a doublet under $SU(2)$) is introduced, with a Lagrange density of

$$\mathcal{L} = (\partial_\mu \Phi)^\dagger (\partial^\mu \Phi) - V(\Phi) = (\partial_\mu \Phi)^\dagger (\partial^\mu \Phi) - (\lambda (\Phi^\dagger \Phi)^2 + \mu^2 \Phi^\dagger \Phi). \quad (2.13)$$

The lagrangian consists of two terms: the first gives the coupling to the gauge field while the second is the potential of the Higgs field. μ^2 is given in units of mass squared and the λ term can be interpreted as quartic self-coupling with the dimensionless positive parameter λ . There are three cases shown in Figure 2.2, μ^2 can be smaller than zero, greater than zero or of course also possible equal zero. If μ^2 is greater than zero the potential is minimal for $\Phi^\dagger \Phi = 0$, i.e. if $\Phi = 0$, and is symmetric around the minimum. The case μ^2 smaller than zero is more interesting and often called "Mexican hat" because of its shape.

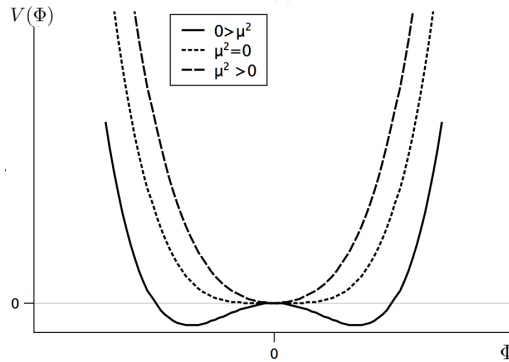


Figure 2.2: Higgs potential

It has an infinite number of states with minimum energy, that fulfil the equation:

$$\Phi^\dagger \Phi = \Phi_1^2 + \Phi_2^2 = -\frac{\mu^2}{2\lambda} = v. \quad (2.14)$$

We may choose $\Phi_1 = v$ and $\Phi_2 = 0$ and look at fluctuations η and ξ around the vacuum, defined by

$\eta = \Phi_1 - v$ and $\xi = \Phi_2$. The lagrangian then is given by

$$\begin{aligned} \mathcal{L}(\eta, \xi) = & \left[\frac{1}{2}(\partial_\mu \eta)(\partial^\mu \eta) - \lambda v^2 \eta^2 \right] + \left[\frac{1}{2}(\partial_\mu \xi)(\partial^\mu \xi) \right] \\ & - \left[\lambda v \eta^3 + \frac{1}{4} \lambda \eta^4 + \frac{1}{4} \lambda \xi^4 - \frac{1}{4} \lambda v^4 + \lambda v \eta \xi + \frac{1}{2} \lambda \eta^2 \xi^2 \right] \end{aligned} \quad (2.15)$$

The first term describes a massive scalar particle η with mass

$$m_\eta = \sqrt{2\lambda v^2} = \sqrt{-2\mu^2} > 0 \quad (2.16)$$

and the second term a massless particle ξ , the so-called Goldstone boson.

Higgs Mechanism

Breaking a local gauge invariance instead of the global gauge invariance makes it possible to choose a gauge in such a way that the Goldstone boson disappears. Now replace the derivative by the 'covariant' derivative associated to $SU(2)_T \times U(1)_Y$

$$D_\mu \Phi = (\partial_\mu + igW_\mu - \frac{i}{2}g'B_\mu)\Phi. \quad (2.17)$$

In the same way like before with identifying η as the Higgs boson h we get

$$D_\mu \Phi = (\partial_\mu + igW_\mu - \frac{i}{2}g'B_\mu) \frac{1}{\sqrt{2}} \begin{pmatrix} 0 \\ v + h \end{pmatrix} \quad (2.18)$$

which can be inserted in the lagrangian

$$\mathcal{L} = (D_\mu \Phi)^\dagger (D^\mu \Phi) - V(\Phi) \quad (2.19)$$

where the from $(D_\mu \Phi)^\dagger (D^\mu \Phi)$ resulting terms can be categorised by

1. ($\propto v^2$)-terms: mass terms for the gauge bosons
2. ($\propto vh$)-terms and ($\propto h^2$)-terms: interaction terms gauge boson with the Higgs

The in nature observed gauge bosons W^\pm, Z, γ can not be matched directly to these B_μ , and W_μ fields, but are built from linear combinations of them:

$$A_\mu = B_\mu \cos \Theta_W + W_\mu^3 \sin \Theta_W \quad (2.20)$$

$$Z_\mu = -B_\mu \sin \Theta_W + W_\mu^3 \cos \Theta_W \quad (2.21)$$

$$W_\mu^\pm = \frac{1}{\sqrt{2}}(W_\mu^1 \mp W_\mu^2) \quad (2.22)$$

with masses emerging directly from the spontaneous symmetry breaking of

$$m_W = \frac{1}{2}g\nu \quad m_Z = \frac{1}{2 \cos \theta_W}g\nu = \frac{m_W}{\cos \theta_W} \quad m_\gamma = 0. \quad (2.23)$$

Two new parameters either μ and λ or m_H and ν are added to the Standard Model by the Higgs mechanism.

2.4 Running Coupling

The coupling constants are not constant, they are energy dependent. Note that in case of QED the effective coupling increases as the momentum increases, while for QCD the coupling decreases with increasing energy. The behaviour of the QCD coupling constant can also be used to explain why we have never seen quarks or gluons as free particles. At short distances the quarks and gluons only couple weakly and therefore can be approximately considered as free, but with increasing distance the effective coupling grows and they have to be considered as bound particles, this effect is called Asymptotic Freedom. Removing a quark (or gluon) from a hadron therefore requires more and more energy as we attempt to pull the quark away. At some point the energy contained in the binding energy is large enough to create a new quark pair, resulting in more colourless hadrons instead of an isolated quark.

2.5 Limitations of the Standard Model

The Standard Model of Particle Physics does include all up to now observed particles and three out of the four fundamental forces and predictions made match successfully with measurements. However the Standard Model also leaves a lot of unsolved problems and fundamental questions.

Gravity is not included in the Standard Model. With a strength of 10^{-42} gravity is 10^{32} orders of magnitude smaller than all other forces, therefore it can be neglected for low center-of-mass energy in comparison to the Planck mass, but if the energy becomes comparable to the Planck mass self-gravity effects of the system can no longer be neglected. The dynamics become non-linear because the dynamics of the state depends on the state itself.

Another problem is that measurements of the cosmic microwave background (for example with the WMAP [7]) suggest that only 4.6% of the universe consists of atoms and therefore can be explained by the Standard Model, while 24% are co-called "dark matter" and 71% "dark energy".

There are some unanswered questions left like: Why is gravity so weak? Why are there so many free parameters? What is the origin of the mass of the neutrinos? Where does the observed baryon anti-baryon asymmetry in the universe come from? Why are left-handed fermions in SU(2) doublets and right-handed in SU(2) singlets? ...

But several attempts were made to solve these problems within new or advanced theories such as for example super-symmetric models like the Minimal Supersymmetric Standard Model [8] in which a symmetry is postulated giving every fermionic particle also a bosonic partner with similar properties but different spin and vice versa.

The ATLAS Experiment

The LHC (Large Hadron Collider) is a proton-proton ring accelerator near Geneva with a circumference of about 27 km. It was first put into operation in 2008 with a center-of-mass energy of about 2 TeV. In 2012 LHC was running with a center-of-mass energy of 8 TeV. After LHC's first long shut down it is expected to reach its full design energy of 14 TeV center-of-mass energy. Two proton beams are accelerated in separated ultra-high vacuum tubes and can be diverted so that they cross at four interaction points, the centres of four large detectors. One of these detectors is a general-purpose detector called ATLAS (A Toroidal LHC ApparatuS), which covers studies from the search for the Higgs boson to super-symmetry and extra dimensions.

The ATLAS detector [9] (Figure 3.1) is 46 m long with a diameter of 25 m and its overall weight is about 7000 t.

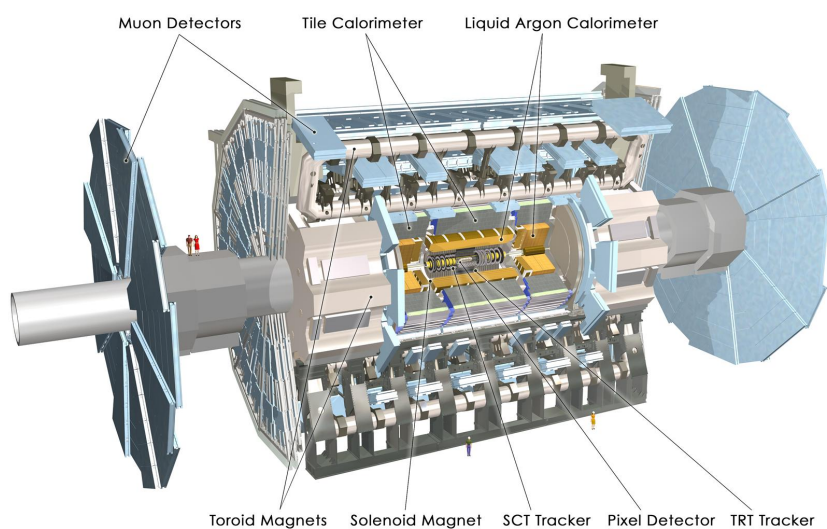


Figure 3.1: schematic ATLAS detector [10]

3.1 ATLAS Coordinate System

In the right-handed ATLAS coordinate system with the z axis orientated along the beam axis. Perpendicular to that is the xy plane with a positive x direction in direction from the interaction point to the center of the LHC ring. The positive y direction is pointing upwards. Additionally to this coordinate system there are some often used parameters defined by:

- transversal momentum p_T
- azimuthal angle ϕ : angle around beam axis $\tan(\phi) = \frac{p_y}{p_x}$
- polar angle θ : angle in regard to the beam axis $\cot(\theta) = \frac{p_z}{p_T}$
- pseudorapidity η : $\eta = -\ln \tan(\theta/2)$
- transverse impact parameter d_0 : distance at the point of closest approach of a track and the primary vertex in the transverse plane
- longitudinal impact parameter z_0 : z -coordinate at the point of closest approach of a track and the primary vertex

3.2 Particle Detection in ATLAS

There are four major components the ATLAS detector [9] consists of. Each of them is providing an essential contribution to the detection and identification of particles.

3.2.1 Major Detector Components

1. Magnet System

There are two magnet systems in ATLAS: the magnet system next to the beam pipe is the so-called central solenoid (CS) with a length of 5.3 m and 2.6 m outer diameter, arranged between Inner Detector and calorimeter to provide the Inner Detector with a 2 T central magnetic field (2.6 T peak magnetic field). The outer toroid system includes the barrel toroid (BT) and two inserted end-cap toroids (ECT) producing a 3.9 T or 4.1 T strong peak magnetic field on the superconductors respectively. The BT consists of eight coils, with a length of 25.3 m and a radial extension from 9.1 m to 20.1 m each, assembled radially and symmetrically around the beam pipe. Also the ECTs are built from eight coils but with a shorter length of only 5 m extending from 1.65 m to 10.7 m radially. Both systems lead to a curvature of trajectories for charged particles, which is necessary to measure the momentum to high precision. All superconduction magnets require appropriate cooling, in case of the CS done by a dewar coupled to the refrigerator, in case of the BT and ECT additional cold helium pumps are used.

2. Inner Detector

Consisting of three parts to provide high resolution measurements at the inner radii but also continuous track measurement at the outer radii, the Inner Detector is the detection system closest to the beam pipe. It measures tracks of short living particles like b hadrons or tau leptons but also of long living particles like electrons. Neutral particles cannot be detected with this detector part. The first layers, arranged as close as possible to the beam pipe ((5 – 12)cm), are pixel detectors consisting of 80 million pixels in three barrel layers and three disks in each end-cap, which enables

three precision measurements over the full acceptance. The next layer is formed by a silicon microstrip tracker, the Semiconductor Tracker (SCT), consisting of 4088 two-sided modules arranged in 4 cylindrical barrel layers and 9 planar endcap disks at each side, providing eight precision measurements per track. The last layer is formed by the Transition Radiation Tracker (TRT) built of straw tubes containing 50000 straws, each divided by two at the center, in barrel and 320000 radial straws in the end-caps, which allows a large number of measurements for each track (typically 36).

3. Calorimeter

To measure energies of hadrons as well as energies of electrons or photons there are two kinds of calorimeters. The electromagnetic calorimeter (ECAL) to measure energies of incoming electrons or photons and the hadron calorimeter (HCAL) for measuring the energies of hadrons like pions. In ATLAS the ECAL is, as the detector parts of the Inner Detector, divided into a barrel and (in this case two) end-caps. It is built as a so called sampling calorimeter which means that it consists of two sorts of alternating layers, absorbers (high density metals) and active elements (liquid argon (LAr)). While interactions in the absorbers create showers, the sensing elements provide a signal that is proportional to the incoming particle's energy. For energy corrections necessary due to loss of energy in material (Inner Detector, coil,...) in front of the calorimeters, both the end-caps and the barrel are complemented with presampler detectors, consisting of thin layers of argon equipped with readout electrodes but without absorbers. The HCAL is composed of the Hadronic Tile calorimeter, the Forward calorimeter and the liquid-argon hadronic end-cap calorimeters (HECs). The tile calorimeter is a large barrel shaped sampling calorimeter, it uses iron layers as absorbing material and scintillating tiles as active material. It consists of one barrel and two extended barrels. Always two independent wheels built from copper plates with an outer radius of 2.03 m form a HEC. The last part of the HCAL is the forward calorimeter made of liquid argon, which is integrated into the end-cap cryostat. The distance to the interaction is 4.7 m.

4. Muon Spectrometer (MS)

In contrast to other particles muons leave the Inner Detector and the calorimeters with only a small loss of energy, therefore an additional detector system is required to measure their momentum [11]. This part of the detector consists of several different detector types. Monitored drift tubes (MDTs) with 1,194 chambers (67000 readout channels) provide a precise track measurement over the range small and medium η , in high η regions and close to the interaction point this is done by 32 cathode strip chambers (370000 channels) due to their higher granularity. Another part of the muon spectrometer is built for triggering and consists of Resistive Plate Chambers (RPCs) in the barrel and Thin Gap Chambers (TGCs) in the end-cap region. The entire muon system is inside of the magnetic field generated by the toroid magnet system.

The covered pseudorapidity regions of the different detector systems can be found in the Tables A.1, A.2 and A.3 in the appendix.

3.2.2 Trigger and Data Storage

Efficient reduction of the enormous amount of data taken by ATLAS to only the physics events of interest is one of the major challenges. At a luminosity of $10^{34} \text{cm}^{-2} \text{s}^{-1}$ with a bunch crossing rate of 40MHz there is far too much data to save. To reduce this abundance of data to events of interest a three stage trigger system is used. The first step, called level-1 (LVL1), reduces the amount of data to about 75 kHz using information from the muon trigger chambers (RPCs and TGCs) and the calorimeters. Events with

designated combinations of high p_T muons, electrons, photons, jets and τ -leptons as well as large total or missing transverse energy (calculated using the combined information) are selected on a time scale of less than $2.5 \mu\text{s}$ and read out from the front-end electronics system into the readout drivers and later the readout buffers.

In the next step, called level-2 (LVL2), the information collected by LVL1 including η , ϕ and p_T of the objects and the energy sum is reused and additionally the LVL2 trigger has access to all event data. However, in the most cases only information from the small fraction of the detector where the objects are located is used. The rate of selected events by LVL2 is about 1 kHz on a time scale from 1 up to 10 ms. The last step is the event filter (EF). The task of this tool is to reduce the selected events by a factor of ten to about 100 Hz. Information from LVL2 is reused and extended with all data relevant to the specific event, applying refined algorithms and selection criteria.

3.3 Particle Identification

Actually what is measured by the detector if a particle is moving through the detector is only a number of hits (except for neutrinos, which have a small probability to interact with matter). Fortunately the distribution and energy deposition of these hits in the detector can tell us a lot about the particle itself. As sketched in Figure 3.2 for some common example particles, different types of particles leave tracks in different regions of the detector.

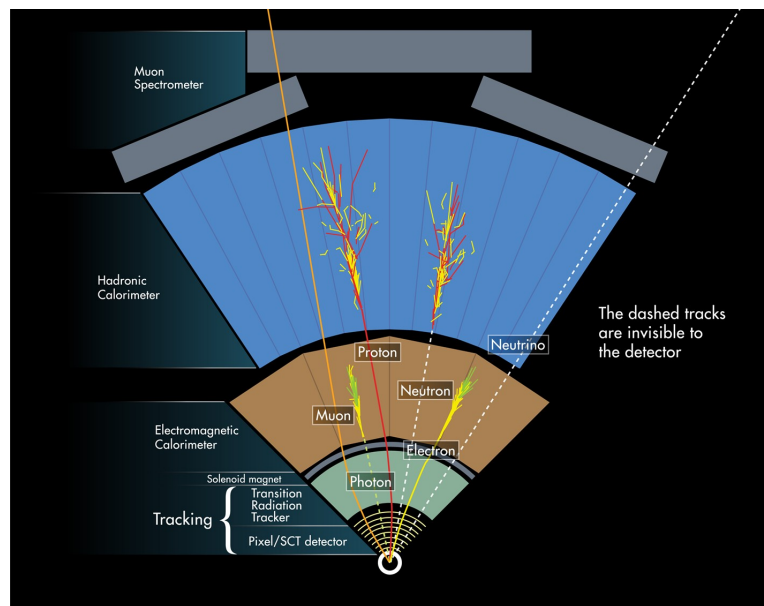


Figure 3.2: Tracks of particles travelling through the ATLAS detector [10]

Short-lived particles often cannot be measured directly in the detector because they do not reach the first detection layer, but their decay products can be measured and the particle can be reconstructed.

3.3.1 Electrons

For the identification of an electron information from reconstructed clusters in the ECAL is associated to reconstructed tracks in the Inner Detector [12]. In this also called track-to-cluster matching it is very

important to also take into account energy loss due to bremsstrahlung. Jets often look very similar to electrons, to avoid these fake electrons cuts on information from calorimeter, tracker and combined calorimeter/tracker information are used. The selection criteria are divided into three steps with increasing rejection power named loose, medium and tight. The loose selection uses information of the second ECAL layer and hadronic leakage (comparison of energy deposited in the hadronic calorimeter and the electromagnetic cluster). Medium cuts additionally use information from first the ECAL layer, track quality and track matching. The tight selection includes additional cuts on the innermost layer of the Pixel Detector barrel region, TRT and conversion rejection, more track matching and tighter quality cuts.

3.3.2 Muons

There are three different approaches to identify muons [11]: the standalone reconstruction using the MS, the combined reconstruction, combining and matching standalone tracks with Inner Detector tracks and the identification of Inner Detector tracks as muons with calorimetric or MS information. In ATLAS these three approaches are combined into two different reconstruction methods called "MuID" and "Staco". Reconstructed muons used in this thesis are reconstructed by the Staco method, this means that two independent measurements (MS & Inner Detector) of the track are statistically combined, taking into account energy losses in the calorimeters. For all pairs of tracks that show reasonable matching in the (η, ϕ) -plane this is proceeded and a limit for acceptance is set. If more than one combination is above the limit the best combination is chosen and two tracks are removed from the considered tracks for new combinations.

3.3.3 Jets

Jet reconstruction is a complex field, on one hand because of the physical effects such as fragmentation, additional underlying events and radiations, on the other hand because of the amount of different detectors, and therefore efficiencies and characteristics, included in the reconstruction process. To reconstruct jets the anti- k_T algorithm [13] is used. In an event consisting of hard and soft particles for each pair of particles distance measures

$$d_{ij} = \min(p_{ii}^{2p}, p_{ij}^{2p}) \cdot \frac{\Delta R_{ij}^2}{R^2} \quad d_{iB} = p_{ii}^{2p}, \quad (3.1)$$

with $p = -1$ are calculated depending on the physical separation $\Delta R_{ij}^2 = (y_i - y_j)^2 + (\phi_i - \phi_j)^2$ (using rapidity and azimuth angle) and the transverse momentum of the particles p_{ii} . If d_{ij} is smaller than d_{iB} the particles i and j are combined to a new particle, otherwise i is declared to be a jet and removed from the particle list. Now the distance measure calculation is started again. The calculated distance is much larger for two soft particles with the same physical separation than for a soft and a hard particle, which leads to the preferred clustering of soft particles to a hard particle.

3.3.4 Missing Transverse Energy (MET)

At hadron colliders the MET plays an important role since the initial center-of-mass energy for a hard scattering is not well known and the energy of escaping neutrinos cannot be measured directly. MET provides the possibility to regain information about the energy carried away by the neutrinos, but can also include instrumental effects like badly measured energies and malfunctioning detector components. In ATLAS the MET is calculated as the negative vector sum of the transverse energy of the electrons,

photons, tau leptons, jets, calorimeter contribution of muons and cells that are not assigned to physics objects or are the remnants of physics objects that have been removed by the ambiguity resolution.

3.3.5 Tau Leptons

Tau leptons are the most difficult leptons to reconstruct because of their short life time and various different decay modes. A tau candidate [14] is a calorimeter jet with a transverse energy larger than 10 GeV within the detector acceptance. To select tracks coming from the tau, tracks within a cone of $\Delta R = \sqrt{(\Delta\Phi)^2 + (\Delta\eta)^2} < 0.4$ around the tau axis are associated to the tau if they pass the quality criteria. Within a cone of $\Delta R < 0.2$ around the four-vector sum of the jet clusters all clusters are used to calculate the tau energy.

To identify hadronically decaying tau leptons a major step is to distinguish tau jets from QCD background. Typically a jet from a tau decay has a low multiplicity and leaves a well-collimated cluster in the calorimeter with only a few associated charged tracks. In ATLAS three different methods are used: a cut-based approach, a projective likelihood method and boosted decision trees (BDT). Variables to distinguish tau jets and other jets are: the jet radius R_{em} (only electromagnetic cells contained in the jet are considered), the fraction of transverse energy ΔE_T^{12} in the calorimeters and the number of charged tracks N_{tr} , exceeding a given transversal energy threshold, each considered in a given ΔR region around the barycenter of the cluster.

It is also possible that an electron is misidentified as a tau, therefore an electron veto is applied (either cut-based or BDT-based).

3.3.6 Overlap Removal

In some cases tracks/energies in the detector were assigned to more than one physical object. To avoid this, an overlap removal has to be applied. It is checked that a cone $\Delta R = \sqrt{\Delta\eta^2 + \Delta\phi^2}$ (with $\Delta R = 0.2$ for muons and electrons otherwise $\Delta R = 0.4$) includes only one object. If more than one object is found, the additional objects are removed, for different types of objects according to the removal order: jet \Rightarrow tau \Rightarrow electron \Rightarrow muon and for the same type of object starting with the lowest p_T , until only one object remains.

3.4 Event Generation and Detector Simulation

Event generation in combination with detector simulation is needed in order to test if a prediction is reasonable or not. The output of the simulation is compared to measured data and checked for deviations. If the model seems reasonable another application of simulation is to use information about the true decay in order to improve reconstruction methods and decrease background due to improved selection criteria. Afterwards these methods and cuts can be used on data. The event generators are all based on Monte Carlo simulation to produce random events with a frequency expected in nature.

3.4.1 Hard Scattering and Underlying Event

An event consists of two major parts: the collision of interest, where two partons collide at high energy and for example create some new high p_T partons, called hard scattering and all other processes called underlying event. The underlying event is comprised of remnants of both beams and multi parton interactions. Sometimes more than one hard scattering process takes place at the same time (or in a time smaller than the readout time of the detector), this is called pile-up. Gluons or photons can be emitted by

the partons, this is called initial or final state radiation (ISR, FSR) depending on the occurrence before or after the hard scattering. FSR is more likely to be detected than ISR since the radiation in most cases is in direction of flight of the parton, which means that ISR is often orientated along the beam axis.

3.4.2 Proton-Proton Scattering Process

In Figure 3.3 the scattering process from incoming protons over hard interaction up to the hadronisation is sketched.

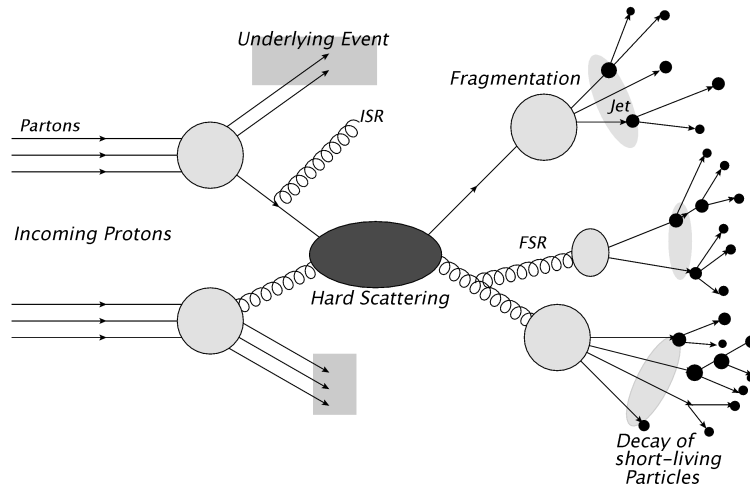


Figure 3.3: Schematic Proton-Proton Scattering Process

1. In the first part each incoming proton can be considered as a bundle of three valence quarks (two up quarks and a down quark) and an additional sea of quark-anti-quark pairs and gluons. At lowest order the probability to find a fixed type of parton with a given momentum fraction is described by the parton distribution function (PDF). This function $f_i(x)$ depends on the energy fraction x of the parton and the momentum transfer between the partons inside one proton Q .
2. The next step is the hard interaction in which electromagnetic and QCD processes take place when the point-like partons collide at high energy, with the possibility to create new high-energy as well as short-lived particles, for instance a Z or Higgs boson.
3. The last part, the hadronisation also called fragmentation, is almost independent from the production reaction. It is described by models tuned to measurements due to the fact that this process is not calculable in QCD, because it is almost completely non-perturbative. In the hadronisation process the colour charge carrying gluons, which decay into quark anti-quark pairs, and quarks are combined in such a way that colour neutral hadrons arise. One model to treat this process is the LUND string fragmentation model [15] where quark and anti-quark are bound together by colour flux lines in form of a tube, inside of this energetic field new quark anti-quark pairs can be created and the tube split into smaller tubes between the quarks unless the energy is reduced to a point where it is not high enough to produce new pairs and so-called primary hadrons are formed. Not all of the primary hadrons are stable, thus further decays take place. Another model is called cluster fragmentation, where parton showering proceeds keeping the colour scheme. Afterwards quarks and anti-quarks are combined to form colour singlet clusters and projected onto high mass meson

resonances. These resonances now decay in either two mesons or a baryon and an anti-baryon unless there is not sufficient energy of the created hadrons for further decays.

3.4.3 Event Generators and Detector Simulation

In experimental particle physics models are tested by generating samples under specified predictions as detailed as could be observed by a perfect detector and comparing these after detector simulation (including detector imperfections) to measured data, therefore the simulated events should on average show the same behavior and fluctuations as observed data. To obtain these generated samples complex simulation tools based on Monte Carlo techniques are used, which also provide the possibility to create samples containing only one kind of reaction.

Event Generators

- **PYTHIA8**

The main general-purpose event generator in ATLAS is PYTHIA [16], which can be used standalone or interfaced with other libraries. Apart from the pp collisions in this thesis discussed, PYTHIA also can simulate incoming $\bar{p}p$, e^+e^- and $\mu^+\mu^-$ beams. PYTHIA can handle around 300 different hard processes, but the produced number of particles in the hard process has to be two or one, in fact only $2 \rightarrow 2$ and $2 \rightarrow 1$ processes are allowed.

At the beginning a collision process, for example the hard process $gg \rightarrow H \rightarrow \tau^+\tau^-$, has to be chosen and calculated in perturbation theory. The next step is the generation of initial- and final-state radiation and the underlying event including multiple parton-parton interactions and beam remnants. The last step, the hadronisation process, is done using Lund string fragmentation (explained in Chapter 3.4.2).

- **POWHEG**

The **PO**sitiv **W**eight **H**ardest **E**mission **G**enerator method is used to produce positive-weighted events with NLO accuracy. One POWHEG framework used in ATLAS is the POWHEG BOX [17] which can be interfaced with several shower handling programs, for example PYTHIA.

- **PHOTOS**

A high precision Monte Carlo generator for bremsstrahlung in decays is PHOTOS [18], which can be interfaced with for example PYTHIA.

- **TAUOLA**

A possibility to handle tau decays with spin effects is provided by TAUOLA [19][20]. Since TAUOLA only handles the tau decay, all other decay parts have to be handled with programs like PYTHIA.

Detector Simulation

- **Geant4**

Geant4 [21] is the standard detector simulation tool of ATLAS providing also a visualisation framework. A geometrical model of the detector is built consisting of a large number of individual components (shape, material) for which all interactions with the particles travelling through are calculated. Additionally "sensitive" elements are defined and the detector responses are simulated.

Higgs and Z Boson at Hadron Colliders

Hadron collider experiments have the advantage of very high reachable beam energy using ring accelerators. While leptons would lose a lot of energy due to radiation the masses of hadrons are much higher and therefore the losses much smaller. In proton-proton collisions heavy particles like Z or Higgs bosons can be produced. The cross-sections and rates as a function of the centre-of-mass energy are shown in Figure 4.1.

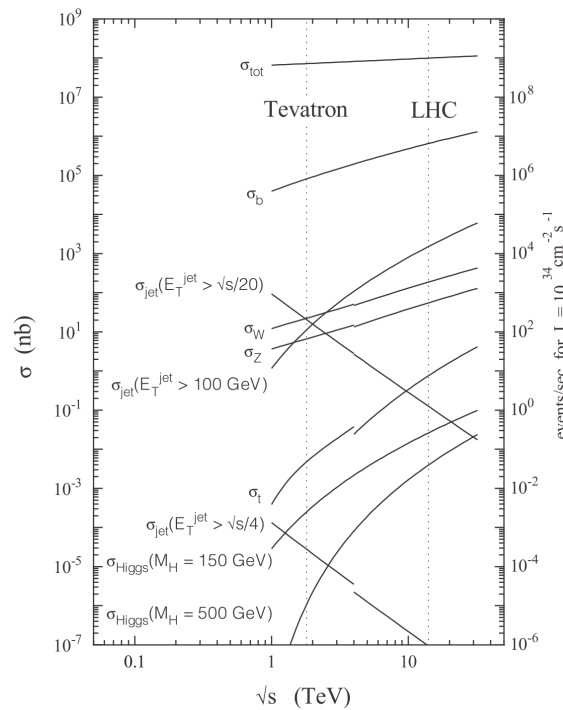


Figure 4.1: Cross-section and rates (luminosity $L = 1 \times 10^{34} \text{ cm}^{-2} \text{ s}^{-1}$) for various processes in proton-(anti)proton collisions, as a function of the centre-of-mass energy [22].

4.1 Z Boson at Hadron Colliders

Scattering between quarks and anti-quarks is the most likely process at LHC to produce a Z boson (shown in Figure 4.2). But virtual photons can be created in the same way, therefore contribution interferences cannot be avoided. The Z boson is a spin-one particle with a mass of about 91.19 GeV and a full width of 2.50 GeV.

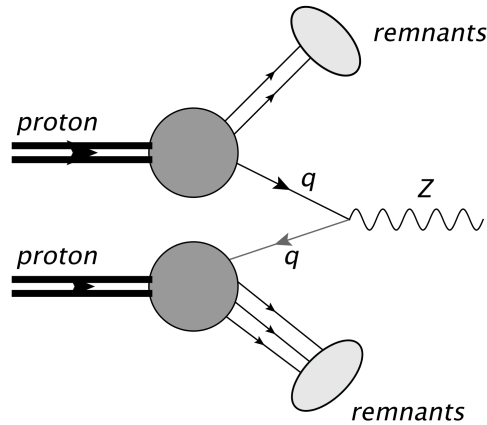


Figure 4.2: Z boson production via quark anti-quark scattering.

Z bosons couple to all kinds of fermions, both left-handed and right-handed but with different strengths. In Table 4.1 the branching fraction for the most common decay modes are given.

decay products	fraction Γ_i/Γ in %
e^-e^+	3.363 ± 0.004
$\mu^-\mu^+$	3.366 ± 0.007
$\tau^-\tau^+$	3.370 ± 0.008
invisible	20.00 ± 0.006
hadrons	69.91 ± 0.006

Table 4.1: Branching fractions for Z boson decays taken from [5].

4.2 Higgs Boson at Hadron Colliders

In Figure 4.3 the Standard Model Higgs boson production cross sections for the relevant production mechanisms, gluon-gluon fusion ($gg \rightarrow H$), vector boson fusion ($qq \rightarrow qqH$), associated production with vector bosons ($q\bar{q} \rightarrow WH/ZH$) and associated production with top quarks ($gg/q\bar{q} \rightarrow t\bar{t}H$), for a large range of Higgs masses at 8 TeV at LHC are shown. The associated width Γ_H depends on the mass $\Gamma_H \propto (m_H)^3$ and is for a mass of $m_H \approx 125$ GeV in the region of a few MeV.

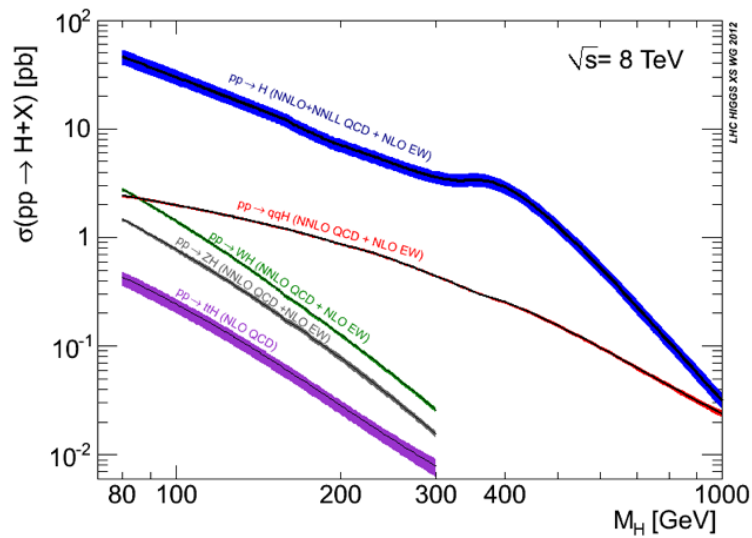


Figure 4.3: Standard Model Higgs boson production cross sections at LHC at 8 TeV. The ggF and VBF processes are calculated in complex-pole-scheme, while other WH/ZH and ttH processes are calculated in zero-width-approximation [23].

Gluon-gluon fusion via an intermediate top quark loop is the dominant production process. With an about one order of magnitude lower cross section at masses below 500 GeV the next probable process is vector boson fusion (VBF). In Figure 4.4 the high related leading-order Feynman diagrams for the production mechanisms are sketched.

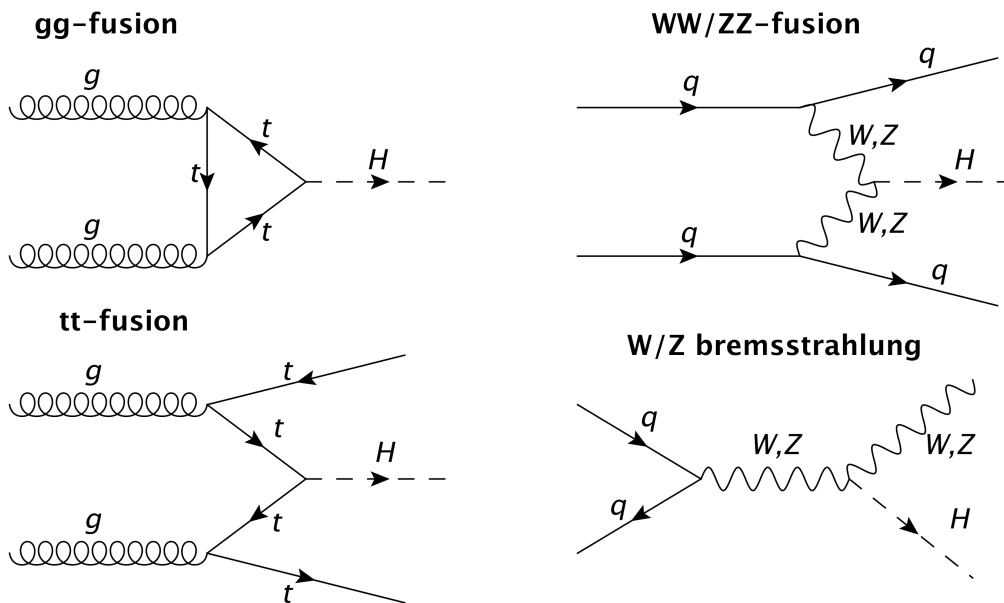


Figure 4.4: Higgs production modes.

The Higgs boson branching ratio depends on the mass of the produced daughter particles. Decays for Higgs masses below 130 GeV are dominated by decays into a pair of b quarks. The next decay into a pair of fermions is the decay into τ leptons, this decay is also the leptonic decay mode with the highest

branching fraction. With increasing mass also decays into pairs of W or Z bosons get more and more interesting since they quickly dominate due to the already mentioned mass dependence. In this thesis a Higgs mass near the experimentally indicated mass region of 125 GeV is assumed.

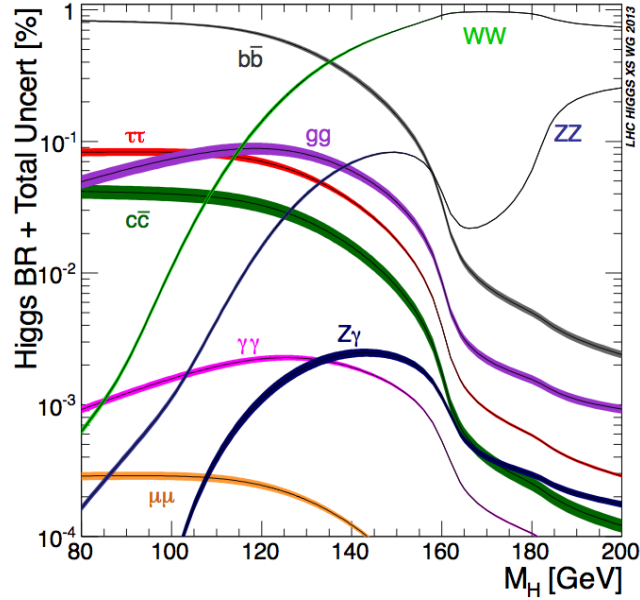


Figure 4.5: Standard Model Higgs boson decay branching ratios at 8 TeV [24].

4.3 Higgs and Z boson distinction and polarisation information

For small Higgs masses, as indicated by the combined research results of 2012 [2], a very promising channel for Higgs searches is the decay into a lepton pair because of the clear signature, which makes it easier to discern events of interest and suppress background. Since the branching fractions of Higgs bosons have a strong mass dependence the previously mentioned decay into tau leptons is preferred to the decay into muons or electrons. Despite the clear signature and a branching fraction of about 6% the Higgs boson has not been observed yet in this channel. A very problematic background in all leptonic channels originates from Z bosons also decaying into two leptons because the event topology is the same as the one for a decaying Higgs boson. A difference between Higgs and Z bosons is their mass, which can be reconstructed as the tau-tau invariant mass. A result from the boosted category from the $H \rightarrow \tau_{\text{lep}}\tau_{\text{had}}$ channel for the 8 TeV analysis is shown in Figure 4.6.

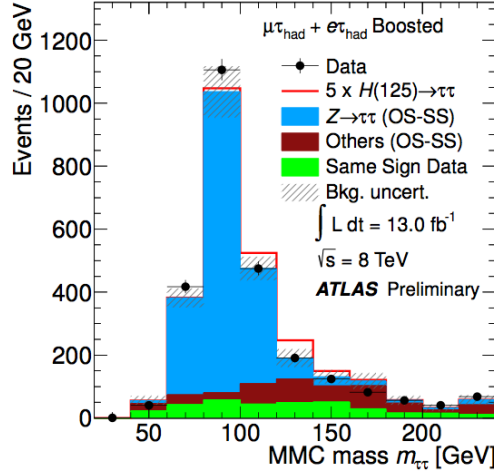


Figure 4.6: mass distributions of the selected events in the Boosted category of the $H \rightarrow \tau_{\text{lep}}\tau_{\text{had}}$ channel for the 8 TeV analysis, estimated using the missing mass calculator (MMC) [25]. The selected events in data are shown together with the predicted Higgs boson signal $m_H = 125$ GeV stacked above the background contributions. For illustration only, the signal contributions have been scaled by a factor of 5. The last bin in the histograms contains the overflow. [4]

It is obvious that even a five times bigger Higgs signal than expected in the Standard Model is very small compared with the large $Z \rightarrow \tau\tau$ background and the background uncertainty. Nevertheless there is hope to see an evidence of $H \rightarrow \tau\tau$ based on the up to now collected data, since it is possible to improve the signal to background ratio via carefully categorised analyses of all relevant final states and the application of multivariate analysis techniques. The difference in the spin of the bosons (1 for a Z boson, 0 for a Higgs boson) might be helpful additional information to improve the separation. For a decaying H/Z boson the cases for resulting tau helicities in the boson rest frame are shown in Figure 4.7. Since the resulting helicities are correlated due to the initial boson spin, they have the same sign for a Higgs boson while they have opposite signs for a decaying Z boson.

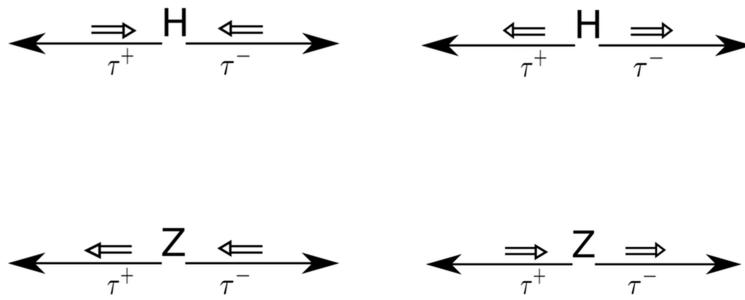


Figure 4.7: Correlation between τ helicities in the decaying boson rest frame for H/Z decaying into a pair of tau leptons. The thick arrows denote the helicities of the tau leptons.

In the next chapter the technical methods to obtain the spin/helicity informations of the tau leptons are discussed.

Tau-Lepton Spin Information

The tau lepton is the heaviest lepton with a mass of 1.777 GeV. As a fermion it carries a spin of $\frac{1}{2}$. Spins are not directly accessible but due to (spin) momentum conservation they have to be conserved. In the tau decay that influences the kinematics of the created daughter particles. Thus the tau decay provides the chance to draw inferences about the initial tau spin/helicity and tau leptons can be used as "spin analysers". Tau leptons and anti-tau leptons will be referred to as tau leptons in the following if not further specified.

5.1 Tau Decays

Due to its high mass the tau lepton is the only lepton which can decay either into leptons or into hadrons (as shown in Figure 5.1). In Table 5.1 the branching fractions for the most common tau decays are given. The total leptonic branching fraction is about 35% and the total hadronic branching fraction about 65% (50% events with one charged hadron, 15% with three charged hadrons).

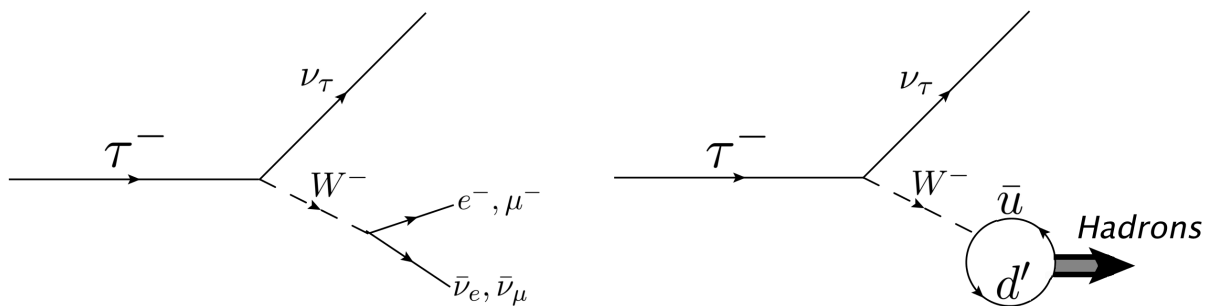


Figure 5.1: Possible τ -decay modes.

decay products	mass meson/lepton	fraction Γ_i/Γ in %
$e^- \bar{\nu}_e \nu_\tau$	0.511 MeV	17.82 ± 0.04
$\mu^- \bar{\nu}_\mu \nu_\tau$	106 MeV	17.39 ± 0.04
$\pi^- \nu_\tau$	140 MeV	10.91 ± 0.07
$\rho^- \nu_\tau$ $\rightarrow \pi^0 \pi^- \nu_\tau$	776 MeV	25.94 ± 0.09
$\pi^0 \pi^0 h^- \nu_\tau$		9.51 ± 0.11
$h^- h^+ h^- \nu_\tau$		9.80 ± 0.07

 Table 5.1: τ -lepton branching fractions taken from [5]. " h^\pm " stands for π^\pm or K^\pm

5.2 Polarisation Information in Simulated Events

In simulation an important tool for handling the tau leptons is TAUOLA [19], in which tau decays are performed regarding to a pre-assigned helicity. This true tau helicity would be an important knowledge for studies concerning the reconstruction of helicity, but unfortunately this information is not saved and therefore not directly available.

Although this is a serious technical problem, there is a possibility to re-establish the event-by-event helicity in simulated events using the true event kinematics and a program based on the same algorithm as TAUOLA called TauSpinner [26].

5.2.1 TauSpinner

TauSpinner [26] is a tool which provides the possibility to recalculate the longitudinal polarisation in any tau lepton sample (data or MC) provided the tau lepton origin is known. In Table 5.2, the probability for the configuration of longitudinal polarisation of the tau leptons from different origins is shown.

Origin	P_{τ_1}	P_{τ_2}	Probability
Neutral Higgs boson	+1	-1	0.5
	-1	+1	0.5
Neutral vector boson Z/γ^*	+1	+1	$p_{\tau z}$
	-1	-1	$1 - p_{\tau z}$

 Table 5.2: Probability for the configuration of longitudinal polarisation of the tau leptons from different origins [27]. The probability of the helicity states $p_{\tau z}$ is a function of the scattering angle and the center-of-mass squared of the hard process.

For each $H/Z \rightarrow \tau\tau$ event TauSpinner calculates a spin weight w_T using the given event kinematics. The weight calculated in the rest frame of the H/Z boson with flight direction of the tau lepton along the z -axis is given by

$$w_T = R_{ij} h^i h^j \quad (5.1)$$

where the h^{ij} are the associated (time and space) components of their respective polarimetric vectors and R_{ij} [19] denotes a matrix describing the full spin correlation between both tau leptons and summing over

both helicities .

$$R_H = \frac{1}{2} \begin{pmatrix} 1 & 0 & 0 & -1 \\ 0 & 1 & 0 & 0 \\ 0 & 0 & 1 & 0 \\ 1 & 0 & 0 & -1 \end{pmatrix} + \frac{1}{2} \begin{pmatrix} 1 & 0 & 0 & 1 \\ 0 & 1 & 0 & 0 \\ 0 & 0 & 1 & 0 \\ -1 & 0 & 0 & -1 \end{pmatrix} = \begin{pmatrix} 1 & 0 & 0 & 0 \\ 0 & 1 & 0 & 0 \\ 0 & 0 & 1 & 0 \\ 0 & 0 & 0 & -1 \end{pmatrix} \quad (5.2)$$

$$R_Z = \begin{pmatrix} 1 & 0 & 0 & -1 \\ 0 & 0 & 0 & 0 \\ 0 & 0 & 0 & 0 \\ -1 & 0 & 0 & 1 \end{pmatrix} \cdot (p_{\tau z} - 1) + \begin{pmatrix} 1 & 0 & 0 & 1 \\ 0 & 0 & 0 & 0 \\ 0 & 0 & 0 & 0 \\ 1 & 0 & 0 & 1 \end{pmatrix} \cdot p_{\tau z} \quad (5.3)$$

$$= \frac{1}{2} \left(\begin{pmatrix} 1 & 0 & 0 & -1 \\ 0 & 0 & 0 & 0 \\ 0 & 0 & 0 & 0 \\ -1 & 0 & 0 & 1 \end{pmatrix} \cdot (1 - P_\tau) + \begin{pmatrix} 1 & 0 & 0 & 1 \\ 0 & 0 & 0 & 0 \\ 0 & 0 & 0 & 0 \\ 1 & 0 & 0 & 1 \end{pmatrix} \cdot (1 + P_\tau) \right) = \begin{pmatrix} 1 & 0 & 0 & P_\tau \\ 0 & 0 & 0 & 0 \\ 0 & 0 & 0 & 0 \\ P_\tau & 0 & 0 & 1 \end{pmatrix} \quad (5.4)$$

P_τ is the polarisation of the single tau lepton in a mixed quantum state and a linear function of the probability of the helicity states $p_{\tau z}$.

$$P_\tau = 2p_{\tau z} - 1. \quad (5.5)$$

The correlation of the spin vector \vec{S} with the polarimetric vector \vec{h} , which is a vector given by the kinematics of the decay and calculated in the respective tau rest frame, can be expressed by [19]:

$$d\Gamma \propto (1 + \vec{S} \cdot \vec{h}) \quad (5.6)$$

meaning that for any decay mode the partial decay width depends on the product of the polarimetric vector and the spin vector. Therefore the most likely configuration for a given S is h pointing in the direction of S and the best estimate of spin direction is the direction of h for which $d\Gamma$ is maximal.

Polarimetric vectors can be calculated for the most common tau decay channels separately using only four vectors of the H/Z , the tau leptons and their decay products. By convention the first component h_0 and R_{11} are set to 1.

In case of a decaying Z boson in the ultra-relativistic limit and neglecting the transverse spin degree this expression can be written as:

$$w_T = 1 + h_{z^+} h_{z^-} + P_\tau h_{z^+} + P_\tau h_{z^-}, \quad (5.7)$$

where h_{z^\pm} is the z component of the polarimetric vector of the τ^\pm . For a neutral spin-zero Standard Model Higgs boson w_T can be written as:

$$w_T = 1 - h_{z^+} h_{z^-} \quad (5.8)$$

Using Equation 5.7 we can calculate the weights for the two polarisation possibilities $\tau_R^- \tau_L^+$ and $\tau_R^+ \tau_L^-$.

$$w_{\tau_R^- \tau_L^+} = 1 + h_{z^+} h_{z^-} - h_{z^+} - h_{z^-} \quad (5.9)$$

$$w_{\tau_L^- \tau_R^+} = 1 + h_{z^+} h_{z^-} + h_{z^+} + h_{z^-} \quad (5.10)$$

For a given longitudinal Z/γ^* polarisation Π this leads to a likelihood for $\tau_L^- \tau_R^+$ of:

$$P_{\tau_L^- \tau_R^+} = \frac{(1 + \Pi) w_{\tau_L^- \tau_R^+}}{(1 + \Pi) w_{\tau_L^- \tau_R^+} + (1 - \Pi) w_{\tau_R^- \tau_L^+}} \quad (5.11)$$

$$= \frac{(1 + \Pi)(1 + h_{z^+} h_{z^-} + h_{z^+} + h_{z^-})}{2 + 2 \cdot h_{z^+} h_{z^-} + 2 \cdot \Pi \cdot h_{z^+} + 2 \cdot \Pi \cdot h_{z^-}} \quad (5.12)$$

In TauSpinner (as in TAUOLA) this probability is compared to a random number between 0 and 1 and if $p_{\tau_R^-\tau_L^+}$ is greater than the number, that the event is assumed to have, the spin configuration $\tau_R^-\tau_L^+$ is assumed else it is assumed to have the spin configuration $\tau_L^-\tau_R^+$.

For a Higgs boson decay the possibility, calculated using Equation 5.1,

$$p_{\tau_R^-\tau_R^+} = \frac{1 + h_{Z^+}h_{Z^-} + h_{Z^+} - h_{Z^-}}{2 - 2h_{Z^+}h_{Z^-}} \quad (5.13)$$

is treated the same way with possible spin configurations $\tau_R^-\tau_R^+$ and $\tau_L^-\tau_L^+$. TauSpinner provides, if the four-vectors of the H/Z boson and the τ lepton information including the four-vectors of the tau lepton itself as well as the created daughter particles (given in pion/kaon end-state) are available, the possibility to calculate an estimate if for example a Z decay looks more $\tau_L^-\tau_R^+$ or $\tau_R^-\tau_L^+$ like. This is done statistically by comparing the calculated probability $p_{\tau_L^-\tau_R^+}$ to a random number. If the random number is greater than $p_{\tau_L^-\tau_R^+}$ the event is assigned to be more likely coming from a $\tau_R^-\tau_L^+$ configuration, if not it is assigned to the $\tau_L^-\tau_R^+$ configuration.

Note that TauSpinner does not return the initial spin configuration but rather an estimate for the initial helicities on a statistical basis.

5.3 Reconstruction of Tau Decay Products

The kinematics of the tau decay products are essential to obtain information about the tau spin, hence it is necessary to reconstruct all decay particles and their four-vectors. as well as possible. Three different neutral pion reconstruction algorithms and two neutrino reconstruction methods, described in the following, were used in this thesis.

5.3.1 Neutral Pion Reconstruction

Neutral pions decay into a pair of photons which leave their energy showering in the ECAL where also a part of the charged pion energy is deposited, making it harder to detect and reconstruct the neutral pion. Three algorithms were used in this thesis to reconstruct the neutral pions.

Cluster-Based Reconstruction

The cluster-based π^0 reconstruction algorithm [28] is available in the 2012 official ATLAS data/Monte Carlo samples. The π^0 counting, done with boosted decision trees (BDTs), is independent of the π^0 vector reconstruction. After a correction for noise and pileup for each cluster the information of the energy of the cluster in the presampler and strip-layer $E_{\text{cluster}}^{\text{PSS}}$, the fraction of energy the cluster has in the hadronic calorimeter $f_{\text{cluster}}^{\text{HAD}}$ and the fraction of energy in the cluster divided by the energy of the calorimeter minus the energy of the tracks $\frac{E_{\text{cluster}}}{E_{\text{calo}} - E_{\text{track}}}$ is used to calculate a so called π^0 score, which is sort of a " π^0 likeliness" given by:

$$\pi^0 \text{ score} = \frac{E_{\text{cluster}}^{\text{PSS}}}{f_{\text{cluster}}^{\text{HAD}} + a \sqrt{\left| \frac{E_{\text{cluster}}}{E_{\text{calo}} - E_{\text{track}}} \right|}}. \quad (5.14)$$

If the number of reconstructed π^0 is greater than zero clusters within a region $\Delta R < 0.2$ of the track system are chosen and corrected for noise. The most likely cluster or pair of clusters to contain the π^0 is

selected, corrected for hadronic energy contamination if necessary and saved. Notice that the number of saved clusters can be two for one π^0 , in this case both clusters are added, and that for more than one π^0 it is not clear which vector corresponds to each π^0 . This method is fast and shows a good efficiency.

Cell-Based Reconstruction

In the cell-based π^0 reconstruction [29] the averaged hadronic shower shapes are used to remove cell by cell π^\pm showers in the ECAL. It is assumed that the energy left by a charged pion in the electromagnetic calorimeter is equal to the energy of the track minus the energy deposited in the hadronic calorimeter. Using Monte Carlo simulations, the longitudinal and lateral shower shapes can be estimated and the expected energy deposit can be removed in the electromagnetic calorimeter. In case of overestimated energy negative energies are assigned. The remaining energy distribution is searched for possible π^0 candidates. The last step is to reduce the fraction of fake π^0 s due to pile up, noise or imperfect subtraction. The subtraction method is independent of the energy distribution in the ECAL and provides the possibility to split the energy in single cells, which is useful for overlapping pion showers.

EflowRec

Reconstruction with EflowRec [30] used in the tau-mode works very similarly to the cell-based algorithm, but the subtraction method in EflowRec removes all energy from the calorimeter clusters around the track until the estimated charged energy is removed instead of subtracting an average value. This is done in ring-shapes around the track in an order depending on the energy distributions in the ECAL and HCAL. The method is robust against statistical shower fluctuations especially if there is no overlap, but leads to an error caused by double counting of energy deposits due to wrong assignments.

5.3.2 Neutrino Reconstruction

Collinear Approximation

The Collinear Approximation (Figure 5.2) assumes that all neutrinos are nearly collinear with the corresponding visible decay products (correct for a strongly boosted tau) and that all the missing energy is due to neutrinos from the tau decay. Therefore, the error of the Collinear Approximation strongly depends on the missing transverse energy resolution.

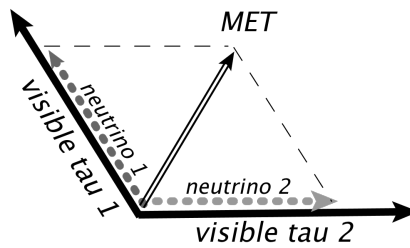


Figure 5.2: Collinear Approximation

At high energies the masses of the particles can be neglected, and we can obtain (using momentum conservation) the equation:

$$\vec{p}_T(\tau_1) + \vec{p}_T(\tau_2) = \frac{\vec{p}_T(\tau_{\text{vis}1})}{x_1} + \frac{\vec{p}_T(\tau_{\text{vis}2})}{x_2} = \vec{p}_T(\tau_{\text{vis}1}) + \vec{p}_T(\tau_{\text{vis}2}) + \vec{E}_{T, \text{miss}}, \quad (5.15)$$

where $x_1 = \frac{E(\tau_{\text{vis1}})}{E(\tau_1)}$ and $x_2 = \frac{E(\tau_{\text{vis2}})}{E(\tau_2)}$ called fractions of visible energy. Then x_1 and x_2 can be expressed as:

$$x_1 = \frac{p_x(\tau_{\text{vis1}}) \cdot p_y(\tau_{\text{vis2}}) - p_y(\tau_{\text{vis1}}) \cdot p_x(\tau_{\text{vis2}})}{p_x(\tau_{\text{vis1}}) \cdot p_y(\tau_{\text{vis2}}) - p_y(\tau_{\text{vis1}}) \cdot p_x(\tau_{\text{vis2}}) + p_y(\tau_{\text{vis2}}) \cdot E_{x,\text{miss}} - p_x(\tau_{\text{vis2}}) \cdot E_{y,\text{miss}}} \quad (5.16)$$

$$x_2 = \frac{p_x(\tau_{\text{vis1}}) \cdot p_y(\tau_{\text{vis2}}) - p_y(\tau_{\text{vis1}}) \cdot p_x(\tau_{\text{vis2}})}{p_x(\tau_{\text{vis1}}) \cdot p_y(\tau_{\text{vis2}}) - p_y(\tau_{\text{vis1}}) \cdot p_x(\tau_{\text{vis2}}) + p_x(\tau_{\text{vis1}}) \cdot E_{y,\text{miss}} - p_y(\tau_{\text{vis1}}) \cdot E_{x,\text{miss}}} \quad (5.17)$$

These equations will be used later. The Collinear Approximation works best if the $\tau\tau$ system is strongly boosted, but $H \rightarrow \tau\tau$ events are often produced with a nearly back-to-back topology according to a small boost.

Missing Mass Calculator (MMC)

The Missing Mass Calculator technique [25] provides the possibility to reconstruct the event kinematics for all $\tau\tau$ event topologies. The requirement to do so is that the orientations of the neutrinos and other decay products have to be consistent with the mass and decay kinematics of a τ lepton. A system of 4 equations with 6 to 8 unknowns (the momentum components of the invisible part of tau decay and for a leptonic decay also the invariant mass of the neutrinos) has to be solved. Since the system is under-constrained it is not possible to give an exact solution, but it is possible to calculate likelihoods for different solutions using additional knowledge like the expected angular distance between the neutrino(s) and the visible tau as probability density functions in a global event likelihood. The final estimator for the invariant tau-tau mass is then calculated by the production of an invariant di-tau mass for all scanned solutions weighted by their probability and extracting the most probable value.

This tool is originally designed for the reconstruction of the invariant di-tau mass but can also be used to reconstruct the neutrino four-vectors or, in the case of a leptonic decay, the sum of the neutrino four-vectors. Since the tool was initially not designed to be used for the neutrino reconstruction, we see to a strong bias in the determined neutrino momentum (Figure 5.3). One reason for that might be that the tool incorporates the expected angle between the neutrino and the visible tau decay products as a probability density function (PDF). This angle is parametrized using the leptonic decay mode and the decay mode with one or three charged hadrons inclusively. From this follows that currently the same parametrisation is used for different hadronic decay modes. Another important issue might be that a PDF is used for the fraction of momentum carried by the neutrino in relation to the momentum of the visible tau decay products. This PDF is obtained from $Z \rightarrow \tau\tau$ decays and therefore can cause a Z -related bias in $H \rightarrow \tau\tau$ decays. As before the used PDF is not decay channel specific. The last point to mention is also the missing transverse energy resolution and the selection cuts might cause biases.

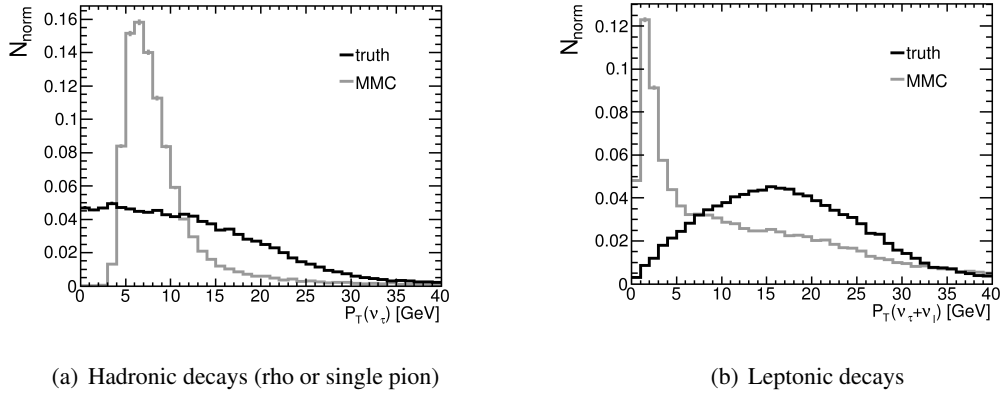


Figure 5.3: Neutrino p_T reconstructed with the MMC compared to its truth value.

5.4 Polarisation Observables in Tau Decays

For each tau lepton the direction of flight and the spin direction, in this case restricted to the helicity of the tau, has to be reconstructed. This is done using the momenta of the tau decay products. Several polarisation observables can be found, each with advantages and disadvantages concerning different decay modes of the tau leptons. In the following the fraction of visible energy, the charged energy asymmetry and polarimetric vectors will be discussed.

5.4.1 Fraction of Visible Energy

A very simple definition to get polarisation information is the fraction of visible energy x . This observable is useful especially for the decay of a tau lepton into a single pion and a tau neutrino, because in that case it is much more likely for the pion to be emitted in the direction of the tau spin orientation. For the example of a decaying τ^- this is sketched in Figure 5.4.

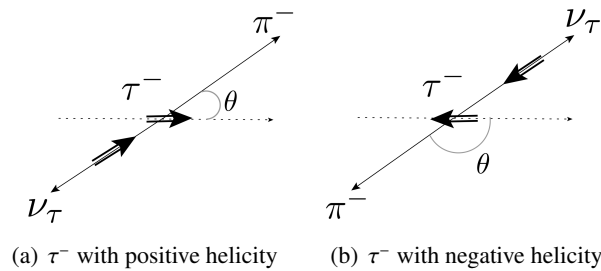


Figure 5.4: Helicities assuming $m_\tau \rightarrow 0$ (denoted by double arrows) for a $\tau^- \rightarrow \pi^- \nu_\tau$ decay where the tau lepton is moving along the dashed line.

This effect is caused by conservation of angular momentum and due to the left-handedness of the neutrino and the spin zero pion. From this follows that it is much more likely for a tau with negative helicity to decay into a low energetic pion with respect to the tau energy and for a tau with positive helicity to decay into a high-energy pion: where P_τ denotes the polarisation of the tau and θ denotes the angle in

the tau rest frame between the tau spin and the pion flight direction [31]:

$$\frac{d\Gamma}{d\cos\theta} \propto \frac{1}{2}(1 + P_\tau \cos(\theta)) \quad (5.18)$$

In terms of $x = \frac{E_\pi}{E_\tau}$, assuming $\beta_\tau \approx 1$ with $a = \frac{m_\pi}{m_\tau}$, it is given by:

$$\cos\theta = \frac{2x - 1 - a^2}{1 - a^2} \quad (5.19)$$

$$\Rightarrow \frac{d\Gamma}{dx} \propto 1 + P_\tau(2x - 1) \quad (5.20)$$

Terms of the order a^2 can be neglected due to the small pion mass. This distribution is shown for tau leptons with positive helicity ($P_\tau = +1$) and negative helicity ($P_\tau = -1$) in Figure 5.5.

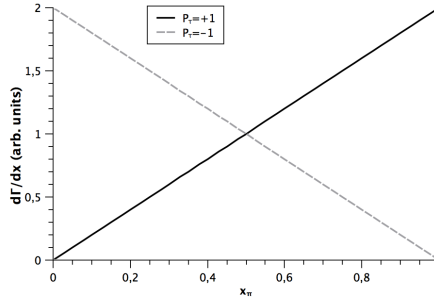


Figure 5.5: $x = \frac{E_\pi}{E_\tau}$ spectrum of pions from polarised tau leptons according to Equation 5.20.

Note that a τ^+ with negative helicity acts like a τ^- with positive helicity and vice versa, since $P_{\tau^+} = -P_{\tau^-}$. A more complicated case is the decay of a tau lepton into a vector meson and a tau-neutrino, because of the spin carried by the meson. One possibility is the creation of a longitudinally polarized rho meson, which means the helicity is zero. In this simplest case the decay is very similar to the single pion case (Figure 5.4) but terms of order a^2 cannot be neglected. The other possibility is the creation of a transversely polarized rho meson shown in Figure 5.6.

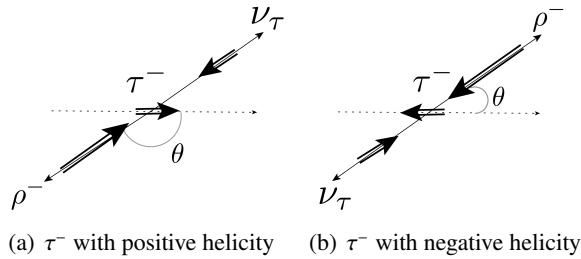


Figure 5.6: Helicities (denoted by double arrows) for a $\tau^- \rightarrow \rho^- \nu_\tau$ decay where the tau lepton is moving along the dashed line with the production of a transversely polarized rho meson.

In the case of a τ^- with positive helicity decaying into a neutrino and a transversely polarized ρ^- it is (because of angular momentum conservation) much more likely that the ρ^- is emitted in the backward direction, while for a τ^- with negative helicity the forward direction is preferred. The distributions can

be expressed by [31]:

$$\frac{d\Gamma_T}{d\cos\theta} \propto 1 - P_\tau \cos(\theta) \quad (5.21)$$

$$\frac{d\Gamma_L}{d\cos\theta} \propto \frac{m_\tau^2}{2m_\rho^2}(1 + P_\tau \cos(\theta)) \quad (5.22)$$

Summing both meson amplitudes leads to a loss of spin information since the information included in the meson polarisation is not considered. This yields for a rho meson:

$$\frac{d\Gamma}{d\cos\theta} \propto \frac{1}{2}(1 + \alpha_\rho P_\tau \cos\theta) \quad (5.23)$$

$$\alpha_\rho = \frac{m_\tau^2 - 2m_\rho^2}{m_\tau^2 + 2m_\rho^2} = 0.46 \quad (5.24)$$

this first expression is similar to the single pion case but with an additional factor α (for a a_1 this factor is $\alpha_{a_1} = 0.12$). The smaller this factor α is the smaller is the sensitivity.

For the spectrum in the laboratory frame (terms of the order a^2 cannot be neglected) this yields [31][32]:

$$\frac{1}{\Gamma_\rho} \frac{d\Gamma_T}{dx_\rho} = b \cdot \left[a^2 \sin^2 \omega + 1 + \cos^2 \omega + P_\tau \cos \Theta^* \cdot (a^2 \sin^2 \omega - a \sin 2\omega \tan \Theta^* - 1 - \cos \omega^2) \right] \quad (5.25)$$

$$\frac{1}{\Gamma_\rho} \frac{d\Gamma_L}{dx_\rho} = b \cdot \left[a^2 \cos^2 \omega + \sin^2 \omega + P_\tau \cos \Theta^* \cdot (a^2 \cos^2 \omega + a \sin 2\omega \tan \Theta^* - \sin \omega^2) \right] \quad (5.26)$$

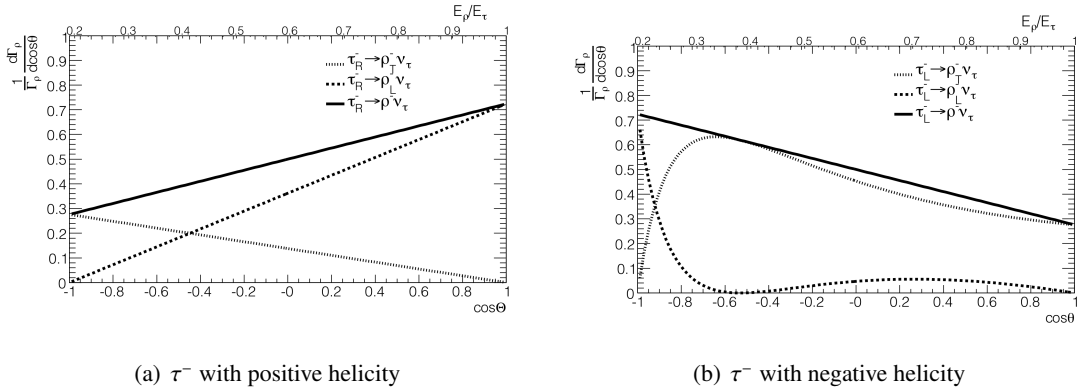
with

$$b = \frac{m_\tau^2 m_\rho^2}{(m_\tau^2 - m_\rho^2)(m_\tau^2 + m_\rho^2)} \quad (5.27)$$

$$\cos \omega = \frac{(m_\tau^2 - m_\rho^2) + (m_\tau^2 + m_\rho^2) \cos \Theta^*}{(m_\tau^2 + m_\rho^2) + (m_\tau^2 - m_\rho^2) \cos \Theta^*} \quad (5.28)$$

$$\cos \Theta^* = \frac{2x - 1 - a^2}{1 - a^2} \quad (5.29)$$

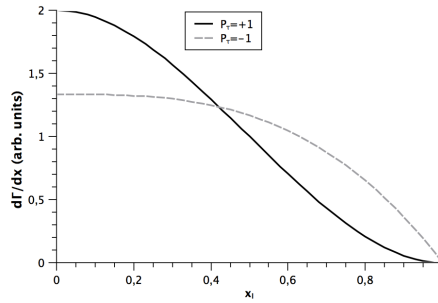
The angular decay distribution divided in transversally and longitudinal rho meson polarisations is shown in Figure 5.7.


 Figure 5.7: The angular decay distribution in the laboratory frame for the decay $\tau \rightarrow \rho\nu_\tau$ [33]

Following from these distributions the leading ρ mesons produced in decays of τ^- with negative helicity are preferably transversely polarised, whereas they are preferably longitudinally polarised for τ^- with positive helicity [32]. An even more challenging decay mode is the decay into a lepton, a tau neutrino and an additional lepton neutrino. In this case all three daughter particles carry spin and the sensitivity decreases sharply, because of the many ways to combine the spins. Another problem is that only the lepton can be observed in the detector, which means there are two undetected particles carrying away an amount of energy where even in the best case only the sum can be reconstructed and therefore the tau rest frame cannot be reconstructed very well. Nevertheless the spectrum can be calculated by integration over the unobservable angle θ and ignoring terms of the order $(\frac{m_l}{m_\tau})^2$ or higher [31]:

$$\frac{d\Gamma}{dx} \propto \frac{1}{3}(1-x) \left[(5+5x-4x^2) + P_\tau(1+x-8x^2) \right] \quad (5.30)$$

and leads to the distributions shown in Figure 5.8.


 Figure 5.8: $x_l = \frac{E_l}{E_\tau}$ spectrum of leptons from polarised tau leptons according to Equation 5.30.

The energy of the tau lepton has to be reconstructed from the neutrino energy and the energy of the visible tau decay products. Thus the quality of the reconstruction of the fraction of visible energy for all decay channels strongly depends on the neutrino reconstruction.

5.4.2 Charged Energy Asymmetry

As mentioned before, for a tau lepton decaying into a vector meson and a neutrino, there is a part of the spin information unused since the decay of the rho meson provides additional information about the spin carried by the ρ meson itself. For the decay of the rho in about 100% of the cases a neutral pion and a charged pion are created (Figure 5.9).

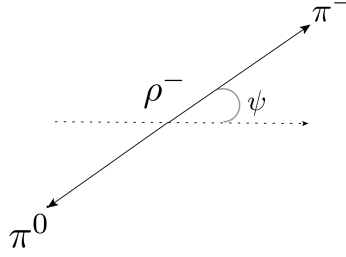


Figure 5.9: Decay $\rho^- \rightarrow \pi^- \pi^0$ where the ρ is moving along the dashed line.

The angle ψ between the direction of flight of the meson and the charged pion, which can be calculated in the laboratory frame [31] to be

$$\cos \psi = \frac{m_\rho}{\sqrt{m_\rho^2 - 4m_{\pi^-}^2}} \cdot \frac{E_{\pi^-} - E_{\pi^0}}{|\vec{p}_{\pi^-} + \vec{p}_{\pi^0}|}, \quad (5.31)$$

is helicity sensitive due to the transformation of the ρ spin into orbital angular momentum since the pions are spin-zero particles. Transversely polarized ρ are more likely to decay into two pions carrying an equal amount of energy, while longitudinally polarised states prefer a large energy asymmetry. To reduce the influences caused by the reconstruction of m_ρ the first term of the equation is dropped, leading to:

$$\Upsilon = \frac{E_{\pi^-} - E_{\pi^0}}{|\vec{p}_{\pi^-} + \vec{p}_{\pi^0}|}. \quad (5.32)$$

This expression is called the charged energy asymmetry and Figure 5.10 shows the resulting distributions. This variable is also usable for a tau decaying into an a_1 but with less distinction power.

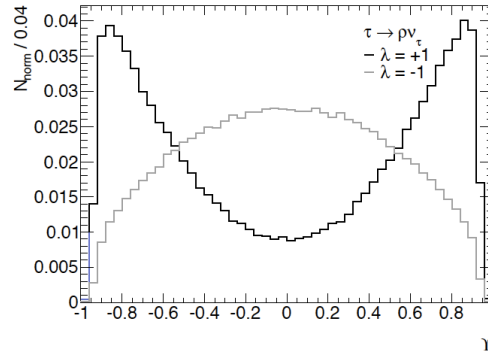


Figure 5.10: The distribution of the charged energy asymmetry, from rho decays divided into left-handed (pink) and right-handed (blue) samples. Each sample is normalized to one [34].

5.4.3 Spin and Polarimetric Vectors

Another way to retrieve helicity information is to use the polarimetric vectors already discussed in Chapter 5.2.1. As in the TauSpinner-Tool only the projection of the polarimetric vector onto the tau flight axis (here denoted as z-axis) is considered. A description how to calculate polarimetric vectors for different tau decay modes can be found in [19]. In this thesis the TauSpinner Tool is used for the calculation. To reconstruct the polarimetric vectors the complete kinematic information for all decay particles need to be available. Thus it is expected that the polarimetric vectors are particularly sensitive to deviations caused by the reconstruction. It is obvious that in case of a leptonic decay the four vectors of both neutrinos are needed but as mentioned in Chapter 5.3.2 only the sum of the neutrinos is reconstructed by the MMC or the Collinear Approximation. The energy of the neutrinos relative to each other depends on the tau polarisation depicted in Figure 5.11, which is the information we try to reconstruct.

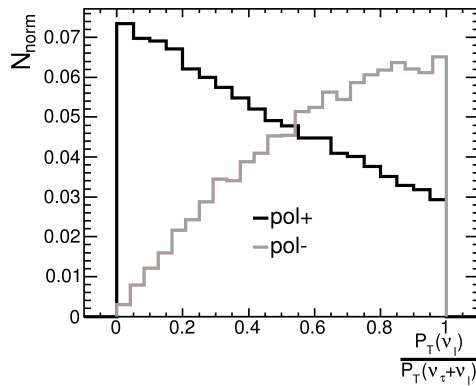


Figure 5.11: Helicity dependence of lepton neutrino transverse energy compared to the total transverse neutrino energy in leptonic tau decays

Because of these problems, unless an improved reconstruction for the two neutrinos in a leptonically decaying tau lepton is found, this channel is not useful for polarimetric vector reconstruction. Fortunately hadronically decaying tau leptons only contain one neutrino among their decay products and a reconstruction is possible.

Analysis

Before looking at the separation power between Higgs and Z bosons decaying into a pair of tau leptons provided by the different helicity correlations, it is useful to start with the examination of effects reconstructing the helicity of single tau leptons. Effects like preselection influences or effects due to reconstruction can be observed and taken into account in terms of the final decay channel choice and the interpretation. After this single tau study the most promising decay channel for the di-tau analysis will be chosen and the separation measured.

6.1 Event Selection

The analysis presented here is based on 2012 Monte Carlo samples containing the decays $H/Z \rightarrow \tau^+\tau^-$, where for technical reasons in the analysis only events with at least one tau lepton decaying hadronically were considered. A list of the used samples can be found in Table 6.1.

process	generator	center-of-mass energy	cross section in [nb]
$H(125 \text{ GeV}) \rightarrow \tau\tau$	PowHeg+Pythia8+Photospp	8 TeV	$1.3170 \cdot 10^{-2}$
$Z \rightarrow \tau\tau$	Pythia8+Photospp	8 TeV	$8.7804 \cdot 10^{-1}$

Table 6.1: Monte Carlo samples used for the analysis. The Z boson sample is an official ATLAS sample revised with additional cell-based and efowRec π^0 reconstruction information

Simulated events are weighted, so that the number of interactions per bunch crossing corresponds to the distribution observed in the ATLAS data. The number of vertices passing the cut criteria has to be at least one and there have to be at minimum of four reconstructed tracks from the primary vertex. Since the Higgs as well as the Z boson are electrically neutral particles, it is required that the tau leptons are oppositely charged. For all events the polarimetric vector reconstruction has to converge and for the parts of the analysis using the MMC it is required that the MMC converges as well.

The cut criteria for the particle selection are summarized in Table 6.2.

particle/object	p_T	$ \eta $	
muon	$\geq 10 \text{ GeV}$	≤ 2.5	$ z_0 \leq 10 \text{ mm}, d_0 \leq 10 \text{ mm}$ combined muon
electron	$\geq 15 \text{ GeV}$	≤ 2.47 , excluded 1.37–1.52	
jet	$\geq 15 \text{ GeV}$	≤ 4.5	
tau	$p_T^{\tau_{\text{had-vis}}} \geq 20 \text{ GeV}$	≤ 2.5	1 or 3 tracks BDT Medium, Unit Charge Electron Veto BDT Medium Muon Veto

Table 6.2: Cut criteria for particle selection

Decays with two hadronically decaying tau leptons as well as with one hadronically and one leptonically decaying tau lepton are considered. The additional channel specific requirements can be found in Table 6.3.

$X \rightarrow \tau_{\text{lep}}\tau_{\text{had}}$	$X \rightarrow \tau_{\text{had}}\tau_{\text{had}}$
At least one BDT medium tau	At least two BDT medium tau
Di-lepton veto	Lepton veto
Number preselected leptons greater zero	Lepton veto
Number preselected tau leptons greater zero	Number preselected tau leptons greater one

Table 6.3: Additional channel specific requirements

The $Z \rightarrow \tau_{\text{lep}}\tau_{\text{had}}$ sample was used for the single tau analysis parts, while for the di-tau analysis the $X \rightarrow \tau_{\text{had}}\tau_{\text{had}}$ samples were used.

6.2 Performance Evaluation

For a complete analysis it is necessary to evaluate which observable and reconstruction method is the most promising. In the helicity separation analysis, where we look at the information of only one tau lepton, the estimation is done by calculating the separation of the one dimensional distributions and the resolution of the reconstruction. In the case of the H/Z separation analysis multivariate methods were used.

6.2.1 Single Tau Lepton Analysis

To estimate the best observable in terms of distinction power between tau leptons with positive and negative helicity as well as to calculate the quality of the reconstruction for each observable two types of information were used:

- The separation $\langle S^2 \rangle$ defined by

$$\langle S^2 \rangle = \frac{1}{2} \sum_y \frac{(\hat{A}(y) - \hat{B}(y))^2}{\hat{A}(y) + \hat{B}(y)}, \quad (6.1)$$

which is the sum over all bins y . $\hat{A}(y), \hat{B}(y)$ are the normalized distributions for the different polarisations. This separation gives an estimation how well τ leptons with negative and positive

helicity can be distinguished.

This quantity indicates how well tau leptons with positive and negative helicity can be separated. For example a value of 1 means that the distributions are completely different, while 0 means that the distributions are identical.

- The standard deviation of the difference (truth-reconstruction) distribution for events with correct reconstructed channel σ_{Δ}

$$\sigma_{\Delta} = \sqrt{(1/N) \cdot \left(\sum_{i=1}^N (\Delta x_i - \Delta \bar{x})^2 \right)} \quad (6.2)$$

with $\Delta x_i = x_i, \text{ truth} - x_i, \text{ reco}$ and number of events N with correctly reconstructed channel. σ_{Δ} can also be understood as the resolution of the reconstruction. This quantity is chosen in such a way that it is invariant under general shifts due to reconstruction, since general shifts do not change the distinction power. For a perfect reconstruction σ_{Δ} would be zero.

6.2.2 Di-Tau Analysis

In order to measure the separation power using information from more than one observable the Toolkit for MultiVariate Analysis [35] implemented in the standard ATLAS analysis data framework 'root' is used. With the search for increasingly smaller effects and rarer particles in high-energy physics the tools to distinguish signal and background events have to become even more efficient. To achieve better distinction power machine learning techniques are used and have become essential for most analysis. MultiVariate Analysis methods (for example rectangular cut optimization, likelihood or decision trees) are used to simultaneously analyse the effects of multiple variables on an outcome of interest. TMVA is a machine learning environment, based on multivariate classification. To run TMVA, a signal and a background training sample with the desired distinction variables are needed. Both samples are then split into a training and testing sample. From the training sample a predetermined number of sub-samples is created and used as input for analysis. In this thesis boosted decision tree classifiers are used.

In the simplest case of a decision tree with monothetic decisions (meaning only one variable is used at every step), shown in Figure 6.1, we are starting with the first decision node using the first discriminating variable x_j to decide if the event is more signal-like or background-like. This decision is then made several times for different variables, not excluding that the same variable is used in several nodes. The tree ends if a given purity in the classification (for background or signal) is reached in a leaf (split sample).

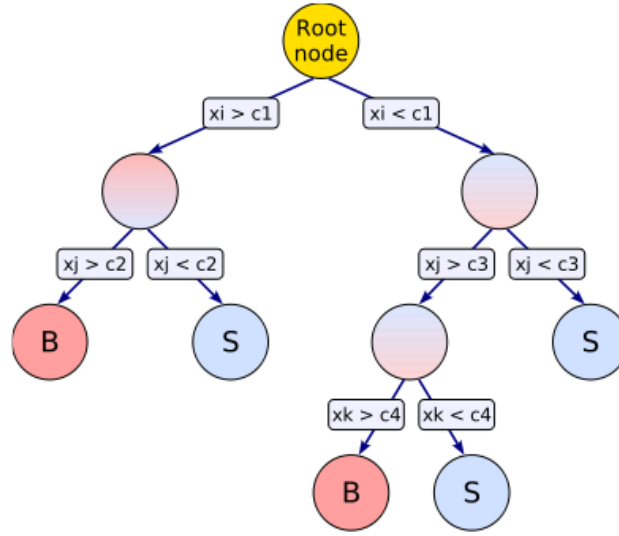


Figure 6.1: Schematic view of a decision tree [35].

Nodes that do not increase the performance are discarded, this is called "pruning", therefore some of the variables might not get used at all. To improve the performance of decision trees several techniques are used, the two most commonly used ones are:

- Bagging

This is a technique to reduce the effects due to statistical fluctuations. From the training set several subsets were built randomly (not excluding that some events might be in more than one set) and trained separately. The average of the output classifiers of all subsets is the final classifier. Due to this averaging single variations are smoothed.

- Gradient Boosting

In gradient boosting each tree can be understood as a summand in a function expansion approach, where the function is assumed to be the weighted sum of the parameterised decision trees. For each tree the parameters are obtained by the minimisation of a so-called loss-function.

A often occurring effect in machine learning is overtraining, meaning that there are too few data points for the number of degrees of freedom of the model. In training samples overtraining seems to improve the classification but used on an independent test sample the effective performance decreases, therefore a comparison of the performance on testing and training sample, is used to detect overtraining. Different MVA methods have different sensitivity for overtraining effects.

For the analysis in this thesis boosted decision trees with gradient boosting "BDT" were used. The provided measures by TMVA for separation power between two samples are:

- separation $\langle S_y^2 \rangle$ of a classifier y , defined by

$$\langle S_y^2 \rangle = \frac{1}{2} \int \frac{(\hat{y}_S(y) - \hat{y}_B(y))^2}{\hat{y}_S(y) + \hat{y}_B(y)} dy \quad (6.3)$$

where $\hat{y}_{S/B}$ are the signal and background PDFs of y .

- significance

Difference between the classifier means for signal and background divided by the squared sum of their root-mean-squares.

6.3 Tau Lepton Helicity Reconstruction

The reconstruction of the true tau helicity is an important step for H/Z distinction based on polarisation information. As the true helicity the helicity reconstructed by TauSpinner running on true decay products and four vectors is used, which yields the correct distributions on a statistical basis.

For the helicity reconstruction the fraction of visible energy, the charged energy asymmetry and the polarimetric vector z-component, presented in Chapter 5.4 are tested in this chapter also to identify effects caused by preselection or reconstruction. It is expected that the fraction of visible energy is affected by the neutrino reconstruction, the charged energy asymmetry by the neutral pion reconstruction and the polarimetric vectors by both types of reconstruction. Note that the separation calculated for the polarimetric vectors might be misleading since the polarimetric vectors are used as an input to estimate the helicity configuration of a given event.

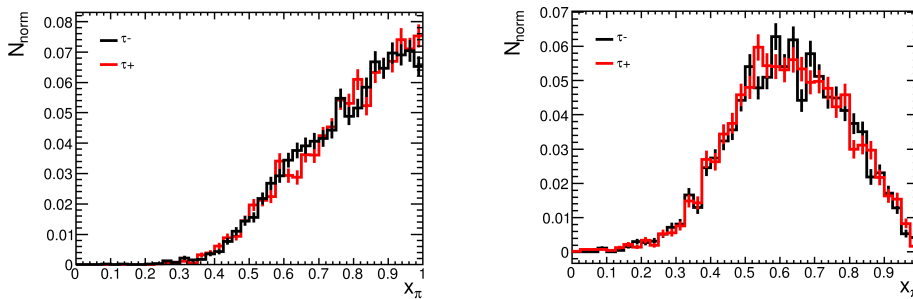
Reconstruction effects can be classified into two groups: effects coming from imperfect four-vector reconstruction and effects coming from not correctly reconstructed decay channels. To distinguish both effects it is useful to apply a so-called truth match on the decay channel, meaning that the reconstructed decay channel is required to be the same as the true decay channel. The observables are compared with regard to their distinction power concerning different tau helicities to chose the most promising combination of observable and tau decay channel.

6.3.1 Fraction of Visible Energy

The fraction of visible energy x is well defined for all tau decay channels, but as seen in Chapter 5.4.1 the distinction power strongly depends on the decay mode. For the most promising decay channel $\tau^\pm \rightarrow \pi^\pm \nu_\tau$ and the decay channel $\tau^\pm \rightarrow l \nu_\tau \nu_l$ the distributions are discussed in the following.

Single Pion Channel

Before looking at reconstruction effects the influences of the preselection have to be considered since the applied cuts on the transversal track momentum (in this case π^\pm momentum) suppresses events with small x values. In the single pion channel this affects especially the distribution of τ^- with negative helicity (τ^+ with positive helicity), where the pion is very likely to have a small energy and is thus strongly influenced by the preselection, whereas the distribution of most likely high-energy pions coming from a decay of a τ^- with positive helicity is barely affected (Figure 6.2).



(a) τ^- with positive helicity, τ^+ with negative helicity (b) τ^- with negative helicity, τ^+ with positive helicity

Figure 6.2: Fraction of visible energy for $\tau \rightarrow \nu_\tau \pi$ decays (truth information).

Since τ^- with positive helicity behave like τ^+ with negative helicity and vice versa, the distributions in the following are split into polarisations "pol" meaning that τ^- with positive helicity and τ^+ with negative helicity are defined as positively polarised tau leptons, whereas τ^- with negative helicity and τ^+ with positive helicity are defined as negatively polarised tau leptons. Figure 6.3 proves that as expected the reconstructed distributions strongly depend on the neutrino reconstruction. The Collinear Approximation as well as the MMC reconstruction strongly deforms the distributions, causing a decrease in distinction power.

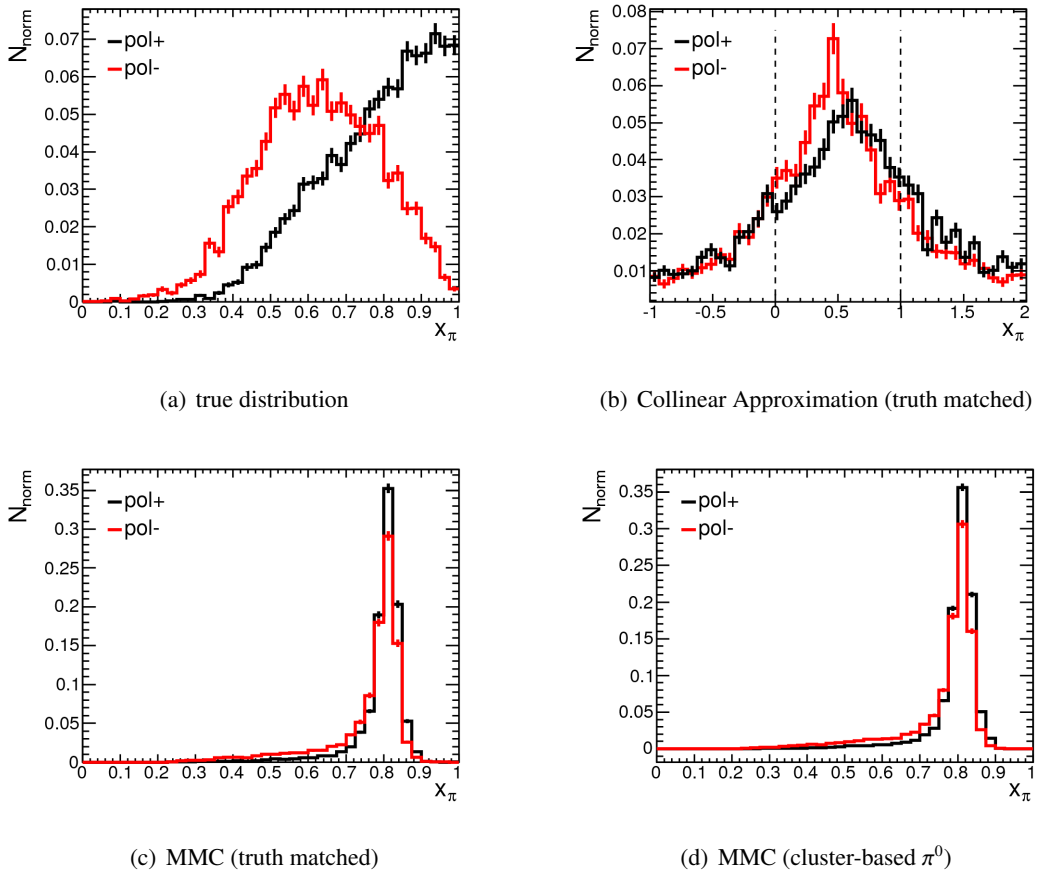


Figure 6.3: Performance of different reconstruction methods for fraction of visible energy, $\tau \rightarrow \nu_\tau \pi$ decays split into tau polarisation.

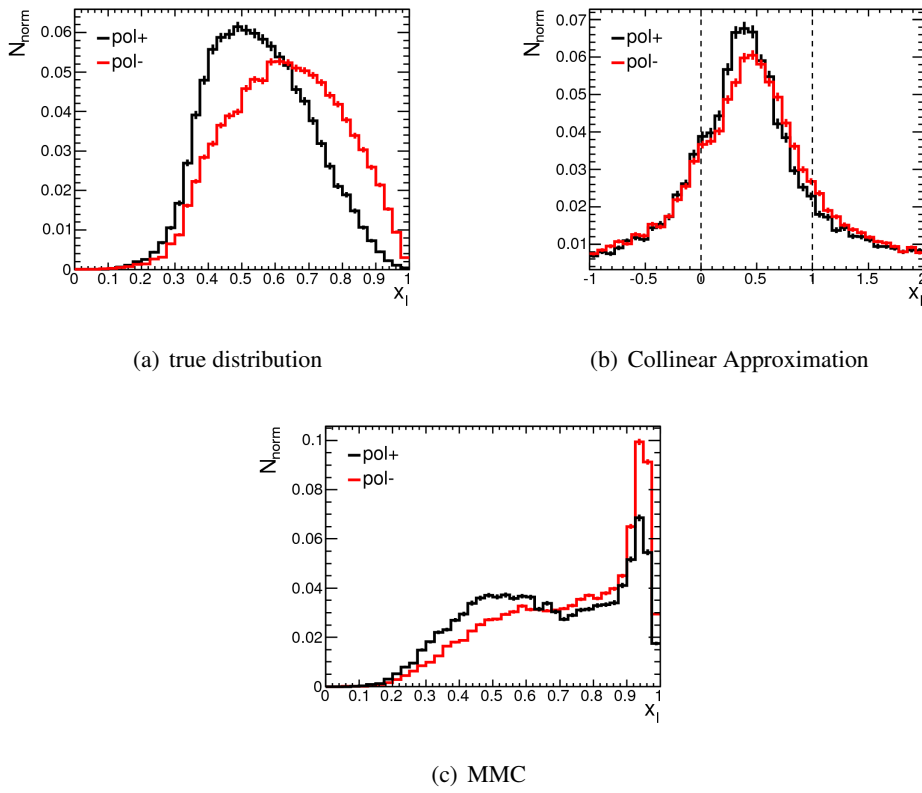
Even though the MMC was not optimized for neutrino reconstruction and has a large bias towards $x_\pi = 0.8$ caused by internal parametrisation it performs better than the Collinear Approximation. In Figure 6.3(d) the additional effect due to the channel reconstruction (cluster-based π^0 reconstruction) can be seen. The discrimination power (Table 6.4) further decreases because of not correctly reconstructed decay modes.

π - channel	truth true	Col. Approx. true	MMC true	MMC reconstr. (cluster-based π^0)
standard deviation σ_Δ		0.634 ± 0.006	0.165 ± 0.001	
separation $\langle S^2 \rangle$	0.203 ± 0.011	0.015 ± 0.004	0.044 ± 0.005	0.041 ± 0.004

Table 6.4: Estimators of the separation power of different x_π calculation methods

Lepton Channel

In Figure 6.4 the x distributions for the decay into a lepton and two neutrinos are shown. Readily identifiable is the effect of the preselection, reducing the amount of events with x between 0 and 0.3 significantly.

Figure 6.4: Performance of different reconstruction methods for fraction of visible energy, $\tau \rightarrow \nu_\tau \bar{\nu}_l l$ decays split into polarisation.

As expected the distinction power is already on truth level smaller than in the single pion channel (Table 6.5) and further decreases with reconstruction.

	truth	Col. Approx.	MMC
standard deviation σ_Δ		0.608 ± 0.002	0.1837 ± 0.0005
separation $\langle S^2 \rangle$	0.039 ± 0.002	0.003 ± 0.001	0.018 ± 0.001

Table 6.5: Estimators of the separation power of different x_l calculation methods

6.3.2 Charged Energy Asymmetry

The polarisation variable which avoids problems with neutrino reconstruction is the charged energy asymmetry with the confinement to events with at least one neutral pion in the final state. The largest distinction power for the charged energy asymmetry is expected in the decay channel $\tau^\pm \rightarrow \rho^\pm \nu_\tau$. The true distributions in Figure 6.5 show that there is an asymmetry effect caused by the preselection cut on the track p_T . This cut is suppressing events with low π^\pm energy, what is especially recognisable in the region between -1 and -0.8 . From the truth distributions a separation of 0.192 ± 0.014 is obtained, which is a little bit lower than for the fraction of visible energy in the single pion channel.

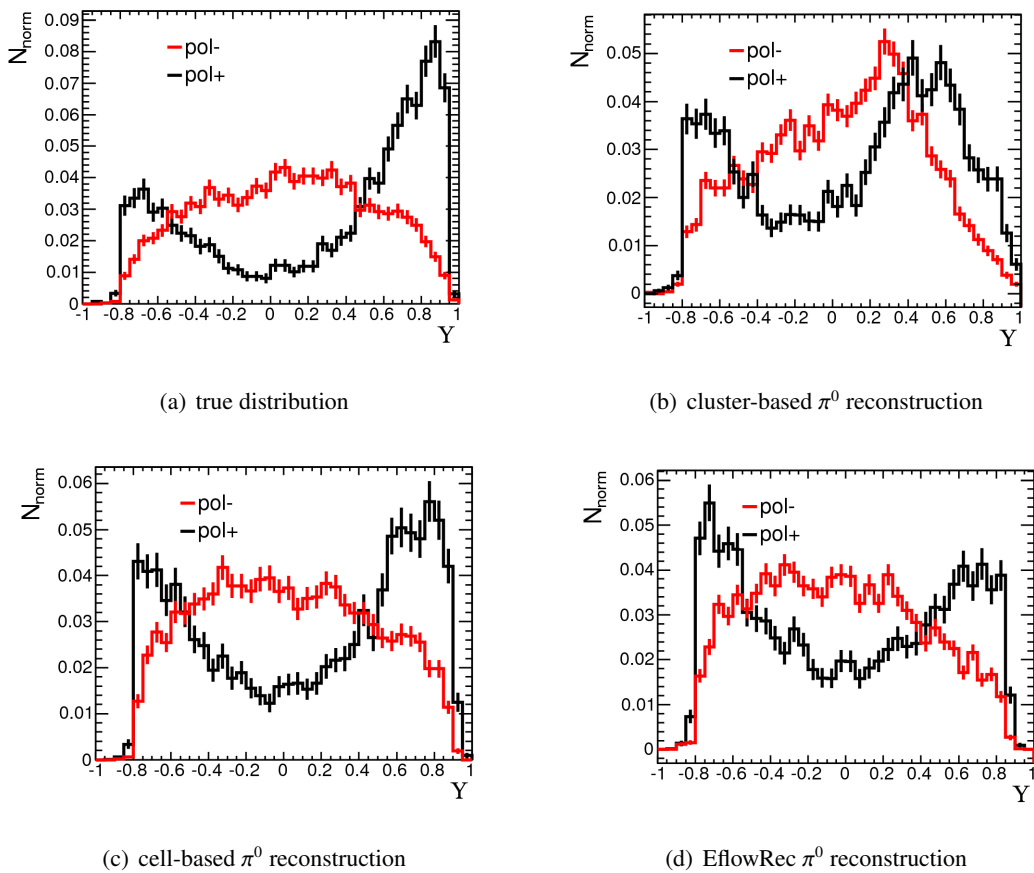


Figure 6.5: Performance of different reconstruction methods for the charged energy asymmetry in $\tau \rightarrow \nu_\tau \rho$ decays.

The reconstructed Υ varies significantly for the different π^0 algorithms and for cluster-based reconstruction a large distortion for the negative polarisation is observed. In addition, plots requiring a true ρ decay (Figure A.1 in the appendix) it is demonstrated that the general form of the distributions is not caused by wrongly classified decay modes, but specific for the respective π^0 energy reconstruction. In Figure 6.6 the event-by-event difference between true and reconstructed Υ is shown and the standard deviation calculated is given in Table 6.6.

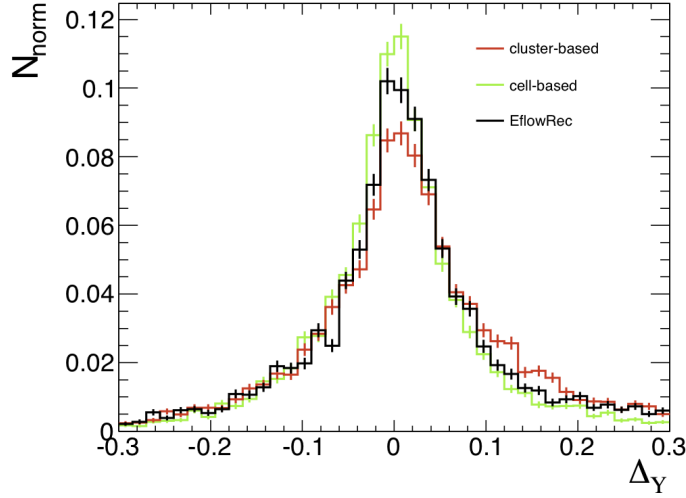


Figure 6.6: Event-by-event difference between true and reconstructed Υ for truth matched $\tau \rightarrow \rho\nu_\tau$ events.

From Figure 6.5 and 6.6 as well as Table 6.6 can be concluded that the most promising π^0 algorithm for the Υ reconstruction is the cell-based method.

	ρ -channel	truth	cluster-based	cell-based	EflowRec
separation $\langle S^2 \rangle$	reconstr.		0.082 ± 0.009	0.109 ± 0.011	0.085 ± 0.009
	truth matched	0.192 ± 0.014	0.113 ± 0.012	0.145 ± 0.016	0.123 ± 0.013
standard deviation σ_Δ	truth matched		0.161 ± 0.002	0.127 ± 0.001	0.165 ± 0.002

Table 6.6: Estimators of the separation power of different Υ calculation methods

Reconstruction using the cluster-based or the EflowRec π^0 gives roughly the same separation. It can be seen that an improved reconstruction of the decay mode, here simulated by truth matching, would improve the separation by roughly 30%. Nevertheless, the obtained reconstructed separation using the charged energy asymmetry is about two times as high as the maximum obtained for the fraction of visible energy in the single pion channel. This makes the ρ -channel even more interesting for polarisation studies.

6.3.3 Polarimetric Vectors

Polarimetric vectors are of special interest since they can be reconstructed in all hadronic channels and use all kinematic information of the decay. As mentioned before, the reconstructed four-vectors of all decay products are needed. Looking at the correlations between H_z and the other polarisation observable gives an insight into the information used to calculate the polarimetric vectors compared to the other observables. Additionally, it provides the possibility to estimate the influences of the preselection. Since in decays into single pions all kinematic polarisation information is comprised in the angle between the charged pion and tau lepton flight direction, which can be replaced by the fraction of visible energy. Therefore, no additional information is gained by using the neutrino four-vector. The expected strong correlation of H_z and x in this channel is reflected in Figure 6.7. Furthermore, the suppression of events with high H_z as an effect of the preselection is readily identifiable.

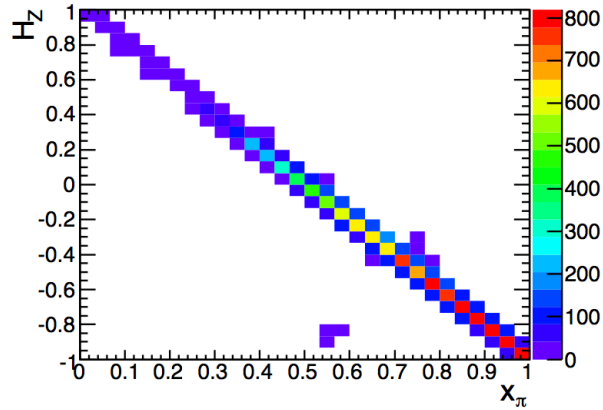
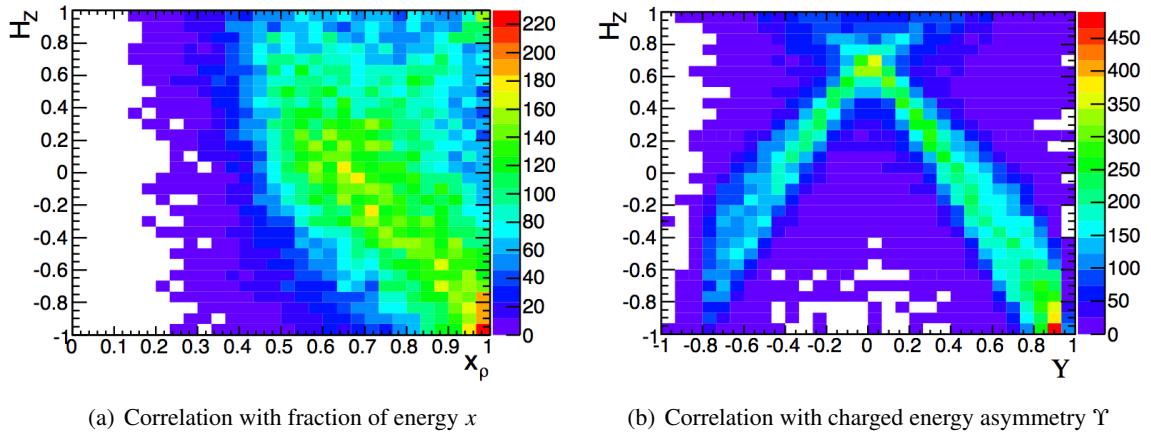


Figure 6.7: Polarimetric vector H_z correlation on truth level with fraction of visible energy x in $\tau \rightarrow \nu_\tau \pi$ decays

In $\tau \rightarrow \nu_\tau \rho$ decays neither x nor Υ uses the full information that is available to H_z , thus the in Figure 6.8 shown correlations are less clear but still recognizable. From both distributions it is obvious that the preselection effects in the H_z distribution will be less obvious for a decay into a ρ meson.



(a) Correlation with fraction of energy x

(b) Correlation with charged energy asymmetry Υ

Figure 6.8: Polarimetric vector H_z correlation on truth level with other polarisation observables in $\tau \rightarrow \nu_\tau \rho$ decays

The quality of the polarimetric vector reconstruction depends on several conditions. First of all the correct decay mode has to be reconstructed, which for hadronic tau decays is a largely relevant problem of π^0 reconstruction. If the decay mode is reconstructed correctly further reconstruction effects associated with the precision of the reconstructed four-vectors have to be considered. The effects can be divided into three groups each concerning one part of the decay objects:

1. track uncertainties
number and four-vector reconstruction of charged pions
2. neutral pion uncertainties
number and four-vector reconstruction of neutral pions (cluster-based)
3. neutrino uncertainties
four-vector reconstruction (MMC)

To analyse the effects of single object types the polarimetric vector reconstruction based on truth information with only one particle type substituted by reconstruction with an additional split into reconstructed (cluster-based) and true number of neutral pions can be found in Figure 6.9. It is obvious that minor deviations coming from track reconstruction are negligible in comparison to deviations due to neutral pion and neutrino reconstruction. Only for the case of correctly reconstructed zero π^0 the track uncertainty is relevant. The polarimetric vector reconstruction very much depends on a correctly reconstructed decay mode, which means the correct number of reconstructed π^0 s. For a wrongly reconstructed number of π^0 s the distribution is shifted caused by either missing or additional energy. A smaller effect related to π^0 reconstruction is arising from deviations in the reconstructed four-vectors in comparison with the true vectors. This effect can be seen in case of one reconstructed and one truth neutral pion in Figure 6.9(d). Uncertainties in neutrino reconstruction are the major problem, especially for no reconstructed neutral pions, where the energy is dispersed among less daughter particles, the distribution is badly deformed. Comparing the rho and single pion decay channel, as expected the influence is larger for the single pion channel than for the rho channel. This can also be explained taking a look at the x distributions in Chapter 5.4 because the average fraction of energy carried away by the neutrino is (summing over both helicities) smaller in case of a decay in a single pion than of a decay in a rho.

In Figure 6.10 the resulting polarimetric vector H_z distributions in the reconstructed single pion and rho channel are shown. The distribution from reconstruction of all decay parts (pointed histogram) is added to the distributions from single track, π^0 or neutrino reconstruction. Table 6.7 displays the estimators for H_z reconstruction in case of zero or one reconstructed neutral pion and one reconstructed charged pion disregarding the true number of pions.

	N(reco π^0)	π^0 , cluster	neutrino, MMC	track
standard deviation σ_Δ	0	0.146 ± 0.001	0.273 ± 0.003	0.0361 ± 0.003
	1	0.236 ± 0.002	0.306 ± 0.003	0.0540 ± 0.0004

Table 6.7: Truth-reconstruction difference standard deviation for polarimetric vector H_z . Only one particle type is reconstructed at the same time, this is either the neutrino using the MMC, the neutral pion using the cluster-based algorithm or the track(s).

The neutrino reconstruction is the part with the largest deviations followed by the neutral pion reconstruction. But it is premature to conclude that the neutrino reconstruction is the largest problem in the polarimetric vector reconstruction, since for example the correlations between the different particle momenta have to be taken into account. Obviously effects coming from the different parts of the reconstruction combine to new previously unseen effects, as for example the peak at $H_z = 0.9$ in Figure 6.10(b).

As appears from Table 6.8 the separations of H_z on truth and reconstruction level for one neutral pion are slightly better than for the fraction of visible energy. This might be caused by the fact that the true polarimetric vectors are used as an input to estimate the helicity configuration of a given event.

	N(reco π^0)	truth	reconstruction (cluster-based & MMC)
separation $\langle S^2 \rangle$	0	0.220 ± 0.010	0.075 ± 0.006
	1	0.272 ± 0.010	0.047 ± 0.004

Table 6.8: Separation of H_z on truth and reconstruction level

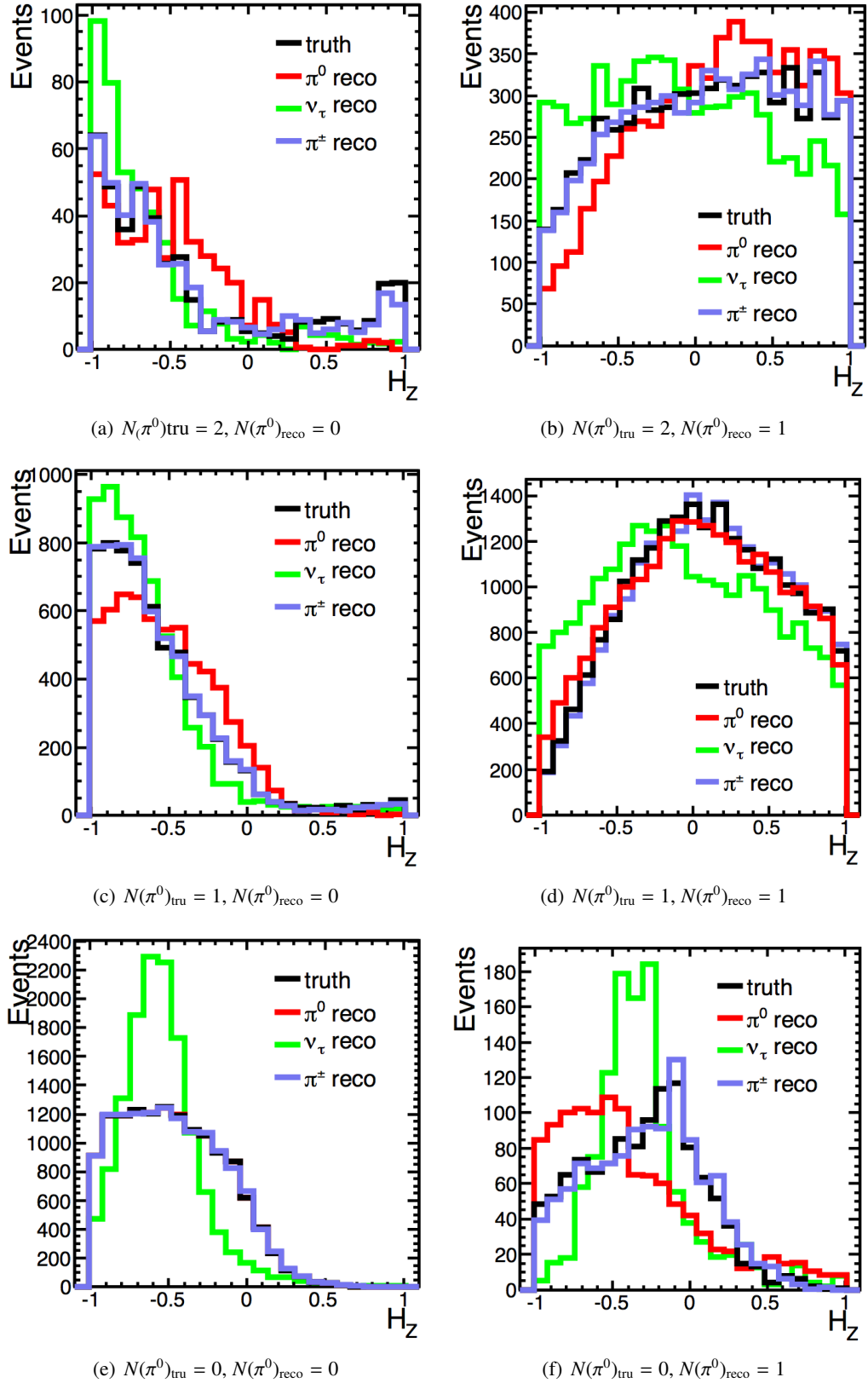


Figure 6.9: Polarimetric vector H_z reconstruction effects split into reconstructed (cluster-based π^0) and true number of neutral pions (1 π^\pm on truth level) respectively. For each of the coloured histograms only one particle type is reconstructed. This is either the neutrino using the MMC, the neutral pion using the cluster-based algorithm or the track(s). The black histogram gives the true distribution.

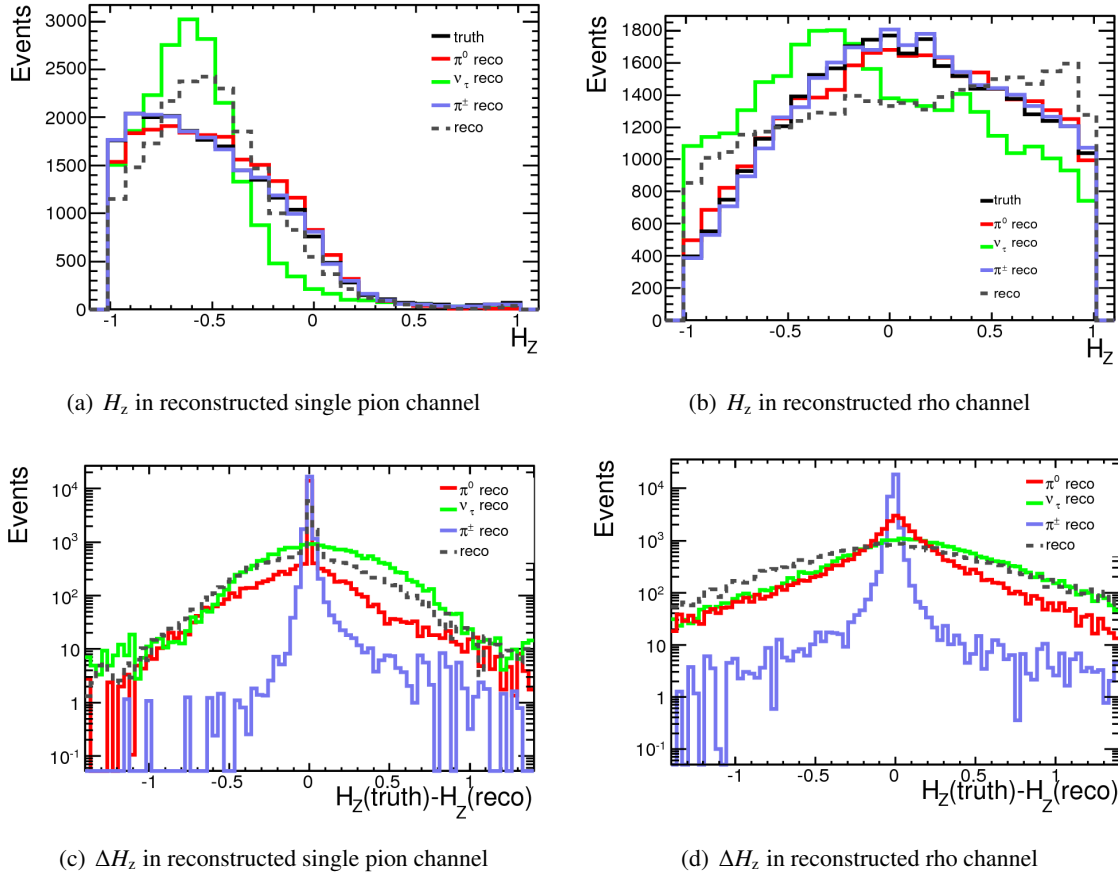


Figure 6.10: Polarimetric vector H_z reconstruction in the reconstructed single pion and rho channel. For each of the coloured histograms only one particle type is reconstructed, this is either the neutrino using the MMC, the neutral pion using the cluster-based algorithm or the track(s). The black histogram gives the true distribution and the dashed histogram the total reconstruction.

6.3.4 Conclusions

For single tau leptons decaying hadronically three different variables were used in order to distinguish the two tau polarisations. As seen in Chapter 5.4 not all variables are equally sensible for each decay channel: for x_π the best channel is the single pion channel and for Υ it is the rho channel. The separation of x_π decreases sharply due to the preselection and the neutrino reconstruction, while the separation of Υ in the rho channel only slightly decreases. Therefore, the $\rho\rho$ -channel seems to be promising for further analysis. For polarimetric vector reconstruction a correct π^0 reconstruction is essential and additional problems occur due to neutrino reconstruction. From single reconstruction effects it cannot be concluded which reconstruction is more problematic for the polarimetric vector reconstruction, since the effects in H_z depend on the overall kinematics and therefore on the correlations.

For single tau decaying leptonically Υ is not usable, this extends to polarimetric vectors due to two not separately reconstructed but needed neutrino four-vectors. The fraction of visible energy x_l can be used in this channel, but the sensitivity is smaller than for the hadronic decay modes.

6.4 Polarisation of H/Z in Monte Carlo Samples

The next step is to combine the information given by both τ leptons and estimate the efficiency for the distinction between H and Z boson. The defined observables are tested considering the maximum achievable separation and the quality of reconstruction, that of course can change due to improvements in future.

6.4.1 Distinction using Truth Information

As mentioned before, in the $\pi\pi$ -channel the best choice on truth level is the fraction of visible energy. The obtained plots in the $\pi\pi$ -channel for fraction of visible energy using the information of both τ leptons can be found in Figure 6.11. The diagrams for the different helicity configurations in the H/Z boson rest frame on truth level are shown, split into polarisations and also the overall behaviour for Higgs or Z bosons. Obviously it is possible to distinguish the different tau lepton helicity combinations. The effect of the preselection explained in Chapter 6.3.1 reduces the expected difference between the distributions of both bosons, but nevertheless the overall distributions look promising.

For the $\rho\rho$ -channel the most promising choice is the charged energy asymmetry (Figure 6.12). Even though the different tau lepton helicity combinations look more separated than in the $x_\pi x_\pi$ diagrams, due to the summation the total distinction power seems to be smaller than for the $\pi\pi$ -channel.

In the $\rho\rho$ -channel also the correlation between the polarimetric vectors is expected to be useful (shown in Figure 6.13). The distributions have much broader maxima than for $\Upsilon\Upsilon$ and especially events with H_Z values around zero will be difficult to separate. Nevertheless the shapes of both distributions are clearly different and the separation for the overall distributions looks very promising.

The results for the separation given in Table 6.9 lead to the conclusion that the best channel on truth level is the $\pi\pi$ -channel with the fraction of visible energy. Since the lepton-hadron channel with a tau pair branching ratio of about 46% plays an important role in the H/Z analysis the same diagram can be found for this channel in the appendix in Figure A.2, although no solution is found yet to solve the two neutrino four-vector reconstruction problem. For the $\rho\rho$ final state the polarimetric vector is more effective than the charged energy asymmetry and the fraction of visible energy in the $\rho\rho$ -channel. An interesting fact is that the fraction of visible energy seems to have a higher separation in the $\rho\rho$ -channel than the charged energy asymmetry even though Υ has a higher separation considering the $\tau \rightarrow \rho\nu_\tau$ decay. A possible reason for that is the summation over both H/Z configurations.

decay channel	x		Υ	H_Z	
	$\pi\pi$	$\rho\rho$	$\rho\rho$	$l\pi&l\rho$	$\rho\rho$
% of $\tau\tau$ -decays	1.19 ± 0.01	6.73 ± 0.03	6.73 ± 0.03	7.68 ± 0.04 & 18.27 ± 0.05	6.73 ± 0.03
$\langle S_y^2 \rangle$	0.189	0.066	0.035	0.075	0.089
significance	0.675	0.373	0.265	0.399	0.433

Table 6.9: H/Z -distinction power for different observables on truth level

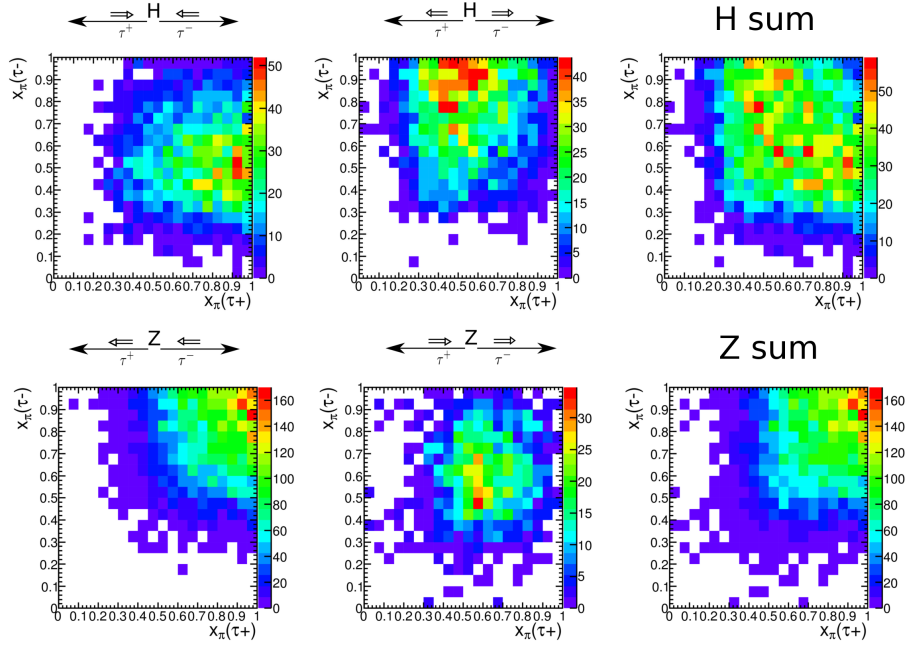


Figure 6.11: Correlation between the fractions of visible energy on truth level divided in helicity combinations and total, $\pi\pi$ -channel. Please note that the color scheme is adjusted to the number of events in the respective plot.

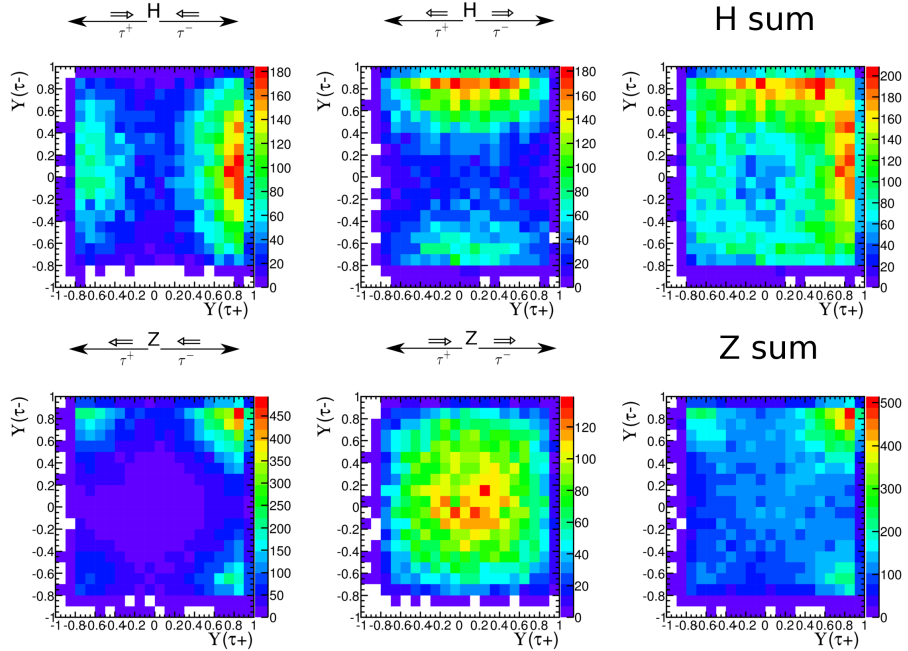


Figure 6.12: Correlation between Υ 's on truth level divided in helicity combinations and total, $\rho\rho$ -channel. Please note that the color scheme is adjusted to the number of events in the respective plot.

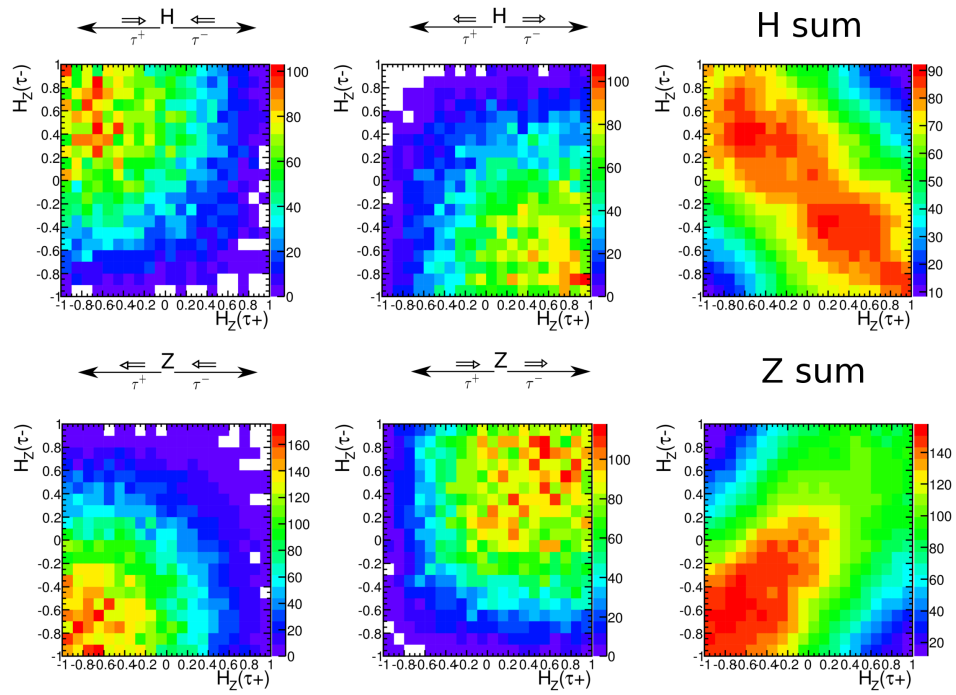


Figure 6.13: Correlation between the polarimetric vectors on truth level divided in helicity combinations and total. $\rho\rho$ -channel. Please note that the color scheme is adjusted to the number of events in the respective plot.

6.4.2 Distinction after Reconstruction

To reconstruct the polarisation of the H/Z boson the four-vector information of both tau leptons and their decay products is needed, unfortunately in the channel with the highest branching ratio (about 46%), the lepton-hadron channel, we have a problem reconstructing the helicity of the leptonically decaying tau due to the two neutrinos in this channel. The channel with the next highest branching ratio of about 42% is the hadron-hadron channel. In the hadronic channels we have seen that on truth level especially the fraction of visible energy in the $\pi\pi$ -channel yield good results. In Figure 6.14 the fraction of visible energy is shown in the reconstructed $\pi\pi$ -channel.

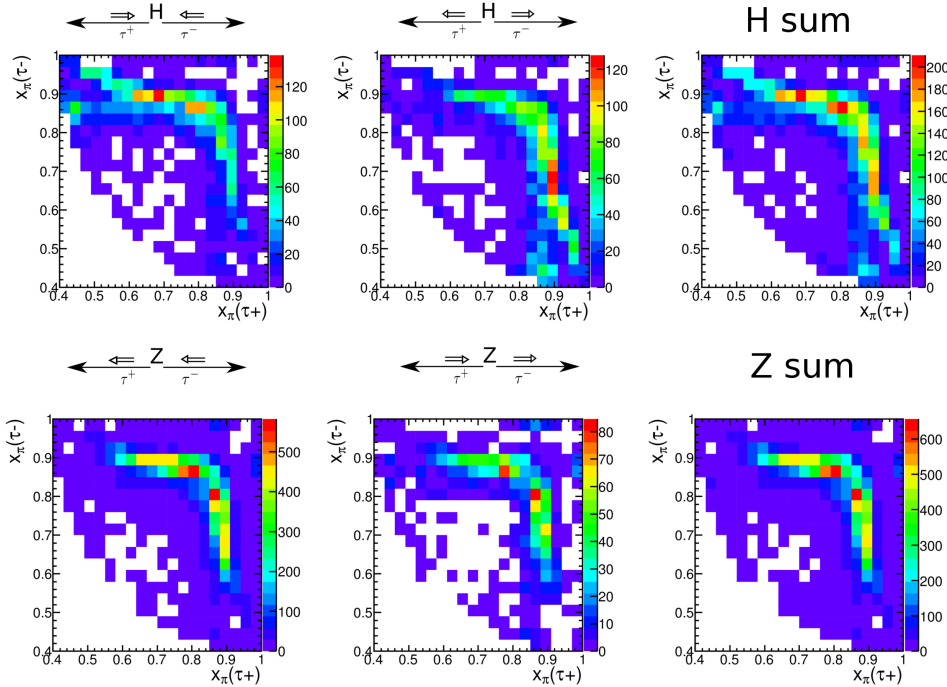


Figure 6.14: Correlation between x_π on reconstruction level divided in helicity combinations and total. $\pi\pi$ -channel. Please note that the color scheme is adjusted to the number of events in the respective plot. (cluster-based π^0 , MMC)

Obviously the previously mentioned effects of preselection and MMC reconstruction lead to a combined loss of events with $x_\pi(\text{reco}) < 0.4$ and a strong shift towards 0.8 – 0.9 resulting from the discussed internal MMC parametrisations.

Looking at reconstructed decays into rho mesons the preferred observables upsilon and polarimetric vector H_Z behave like shown in Figure 6.15 and 6.16.

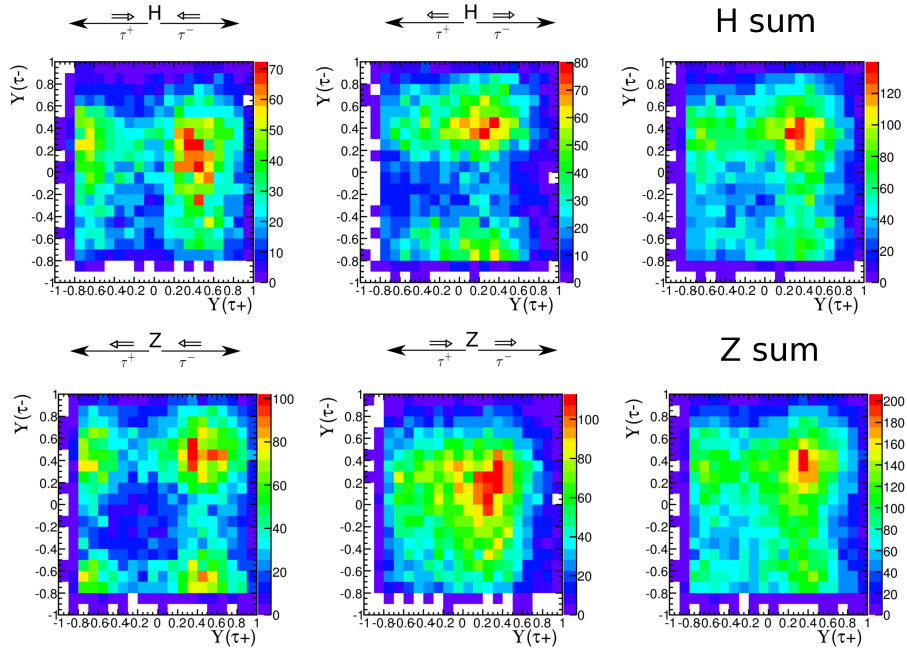


Figure 6.15: Correlation between Y 's on reconstruction level divided in helicity combinations and total. $\rho\rho$ -channel. Please note that the color scheme is adjusted to the number of events in the respective plot. (cluster-based π^0)

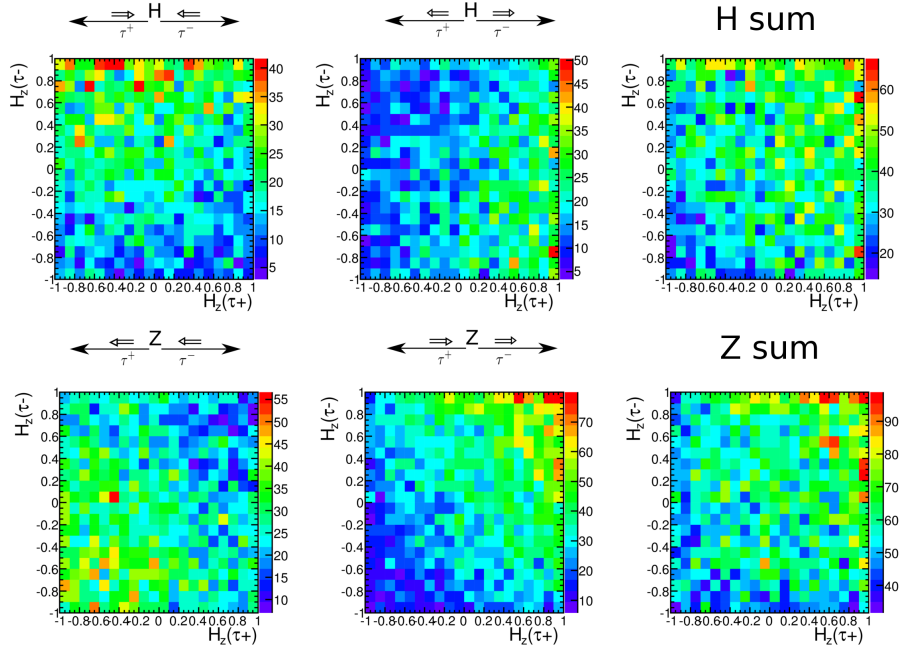


Figure 6.16: Correlation between H_Z s on reconstruction level divided in helicity combinations and total. $\rho\rho$ -channel. Please note that the color scheme is adjusted to the number of events in the respective plot. (cluster-based π^0 , MMC)

As before the distinction power is calculated for the shown decay modes and observables with the values given in Table 6.10. The additional broadening in the distributions due to reconstruction makes the overall distribution using the charged energy asymmetry and also the polarimetric vectors for a Higgs and a Z boson look similar and decrease the separation power sharply.

	x		Υ	H_Z
decay channel (reconstr.)	$\pi\pi$	$\rho\rho$	$\rho\rho$	$\rho\rho$
$\langle S_y^2 \rangle$	0.075	0.56	0.007	0.0004
significance	0.395	0.347	0.092	0.027

Table 6.10: H/Z -distinction power for different observables on reconstruction level

To complete the analysis in the $\rho\rho$ -channel the distributions for the fraction of visible energy can be found in Figure 6.17.

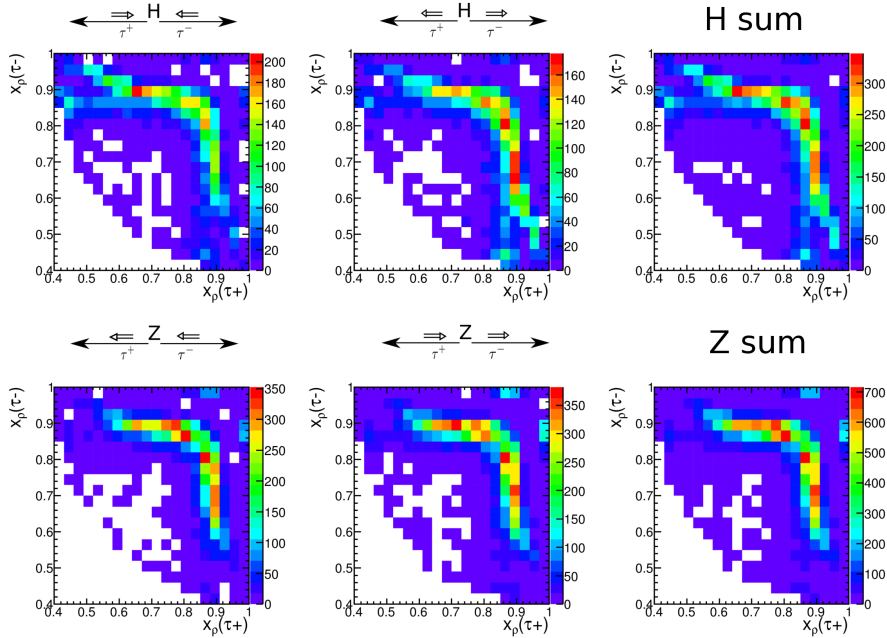


Figure 6.17: Correlation between x_ρ on reconstruction level divided in helicity combinations and total. $\rho\rho$ -channel. Please note that the color scheme is adjusted to the number of events in the respective plot. (cluster-based π^0 , MMC)

In the following chapter an analysis of the polarisation reconstruction combining the observables is performed.

6.4.3 Combined Analysis in the $\rho\rho$ -Channel

Unlike in the $\pi\pi$ -channel it is in the $\rho\rho$ -channel possible to combine information of all observables to optimize the distinction power. The BDT response comparing signal (H bosons) and background (Z bosons) in the test and training sample is shown in Figure 6.18. Both distributions show very good agreement.

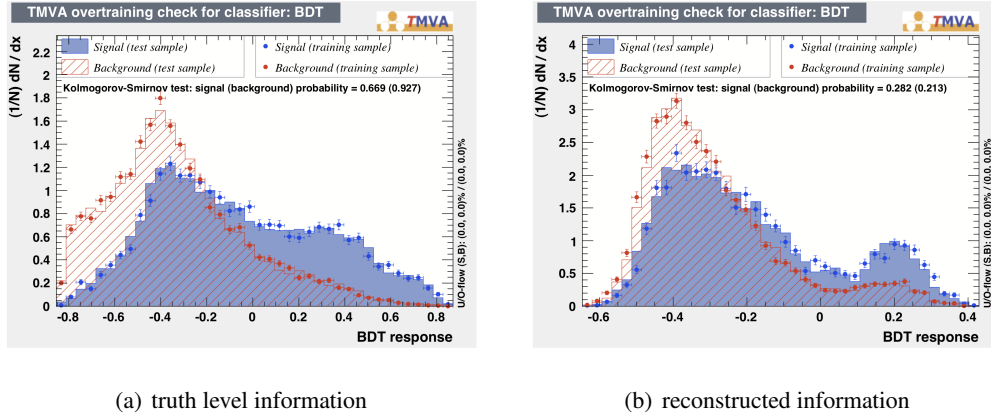


Figure 6.18: BDT response calculated by TMVA for the combination of all observables in the $\rho\rho$ channel.

As expected the reconstruction does not reach the maximal value of the truth information calculation. This is also demonstrated in Table 6.11 showing separation and significance for both MVAs and additional combinations of the observables.

decay channel	truth				reconstruction			
	all	H_Z, x	H_Z, Υ	Υ, x	all	H_Z, x	H_Z, Υ	Υ, x
separation $\langle S_y^2 \rangle$	0.141	0.140	0.094	0.098	0.055	0.055	0.006	0.053
significance	0.563	0.566	0.448	0.458	0.333	0.328	0.065	0.327

Table 6.11: H/Z -distinction power for combination of observables calculated by TMVA for BDT method. The error on the separation and the significance due to the TMVA settings is tested to be in the order of 0.002

The stability of the resulting separation and significance was tested regarding the variation of analysis parameters and the error was found to be in the order of 0.005 for both quantities. On truth level the separation can be improved by a combination of all observables. An equivalent result can be obtained by the combination of H_Z and x . This is reasoned by the fact that these are the best variables (on truth level) in the $\rho\rho$ -channel and H_Z already includes the ρ spin information. Combinations with Υ and an other observable in this channel cannot reach the same separation.

On reconstruction level the observable with the highest separation is the fraction of visible energy, which is reflected by the calculated separations.

6.4.4 Conclusions

The H/Z distinction power for the chosen observables can be improved by combining several observables. The best performance using truth information is reached using the fraction of visible energy and the polarimetric vectors. The separation based on the charged energy asymmetry is low since only the sum of the different helicity combinations for H/Z boson is considered.

On reconstruction level using the MMC and the cluster-based π^0 algorithm the separation of Υ and H_Z is very small since Υ suffers from an additional blurring due to π^0 reconstruction and the polarimetric vector is calculated from all decay products and therefore is sensitive to all miss-reconstruction effects.

Conclusions and Outlook

In this thesis three different observables (the fraction of visible energy, the charged energy asymmetry and the z-component of the polarimetric vector) were tested in several τ decay channels in order to distinguish Higgs and Z bosons. Most promising, looking at truth level information, is the single pion channel, in which the fraction of visible energy can be used as well as the polarimetric vectors, with a strong correlation between both observables. The separation in this channel is very challenging on reconstruction level due to neutrino reconstruction and selection effects. Fortunately, the ρ decay mode provides an observable that is independent of neutrino reconstruction, the charged energy asymmetry. Combining all observables in this channel in a multivariate analysis provides the possibility to retrieve separation power.

It was found that the major problems in the reconstruction of these variables are related to neutrino and neutral pion reconstruction while the track reconstruction works quite sufficiently. For the neutrino reconstruction the Collinear Approximation was used as well as the Missing Mass Calculator. The Missing Mass Calculator is not originally designed for neutrino reconstruction and generates a strong bias in the neutrino energy distribution due to its internal parametrisation. Despite of this bias it turned out to work better. Nevertheless, it would be helpful for further polarisation studies to optimize the Missing Mass Calculator for this purpose.

For the distinction of the different decay channels, necessary to use the optimal polarisation observable for each channel, a neutral pion reconstruction algorithm has to be used. Three neutral pion reconstruction algorithms were tested in the reconstruction of the charged energy asymmetry, of which only the cluster-based π^0 reconstruction is available in ATLAS 2013 data and Monte Carlo. The cell-based π^0 reconstruction and a method named EflowRec, were provided in an ATLAS sample extended with additional π^0 information. The most efficient algorithm in terms of separation between the two tau lepton polarisations turns out to be the cell-based π^0 reconstruction, which shows an about 30% improved separation compared to the cluster-based method. Furthermore there is a new algorithm to improve the π^0 counting, PanTau, and an on-going work on further improvements in the tau-substructure algorithms [29][36]. Since the cell-based method is not available in the common samples further results of this thesis were based on the cluster-based π^0 reconstruction, leading to results which can be expected to be improved by the more efficient method.

For a qualitative analysis concerning the measurement of separation powers in the H/Z distinction this thesis was limited by the available data, to this end additional high statistic samples in the $X \rightarrow \tau\tau \rightarrow \rho\rho$ or $\pi\pi$ channel would be extremely useful.

An extension to other decay channels including leptonic ones might be valuable especially in view of the incorporation into an analysis. The leptonic τ -decay channels, which have the highest branching fractions, provide only small reconstructed polarisation information since the information contained in the four-vectors of two neutrinos can only be partially reconstructed.

For the incorporation into the currently used Higgs analysis, the study needs to be extended to other backgrounds as well. This is a promising aim in view of the start of Run II of the LHC scheduled for 2015, since the amount of data will rapidly increase and polarisation information might be a helpful extension to the already available tau lepton information.

Useful information

A.1 Detector Acceptance in pseudorapidity

system	position	η coverage
pixel	1 removable barrel layer	± 2.5
	2 barrel layers	± 1.7
	5 end-caps (each side)	1.7 – 2.5
SCT	4 barrel layers	± 1.4
	9 end-caps (each side)	1.4 – 2.5
TRT	axial barrel straws	± 0.7
	radial end-cap straws (each side)	0.7 – 2.5

Table A.1: Covered pseudorapidity regions of the Inner Detector taken from [9].

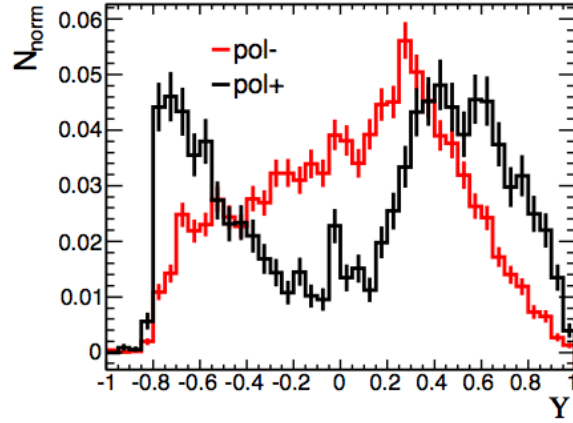
system	position	η coverage
ECAL	barrel	± 1.475
	end-cap (each side)	1.375 – 3.2
Presampler	barrel	± 1.52
	end-cap (each side)	1.5 – 1.8
Hadronic Tile	barrel	± 1.0
	extended barrel	0.8 – 1.7
Hadronic LAr	endcap (each side)	1.5 – 3.2
Forward Calorimeter	forward	3.1 – 4.9

Table A.2: Covered pseudorapidity regions of the Calorimeters taken from [9].

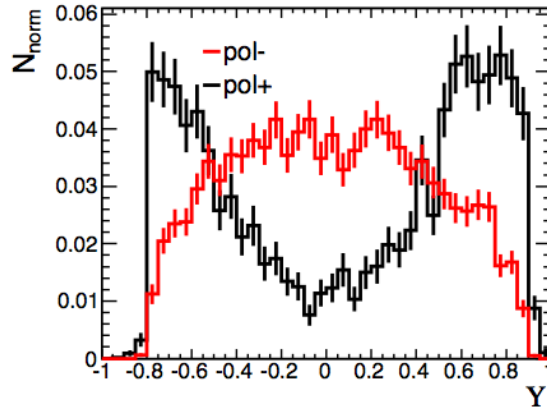
system	position	η coverage
	barrel chambers	± 1
	end-caps (each side)	1 – 2.7

Table A.3: Covered pseudorapidity regions of the muon spectrometer taken from [9].

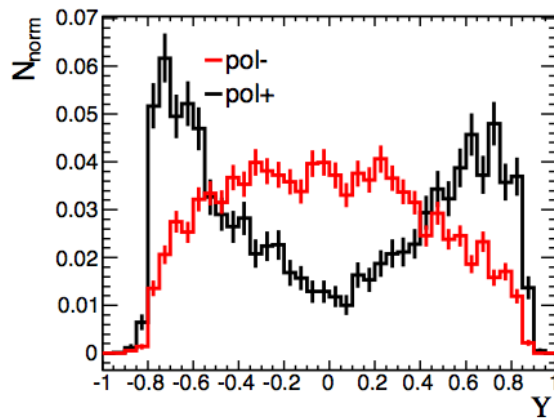
A.2 Charged Energy Asymmetry Reconstruction with Channel Match



(a) cluster based π^0 reconstruction



(b) cell based π^0 reconstruction



(c) eflowRec π^0 reconstruction

Figure A.1: Performance of different reconstruction methods for charged energy asymmetry, $\tau \rightarrow \nu_\tau \rho$ decays split into polarisation for truth matched channel.

A.3 Additional Observable Correlations

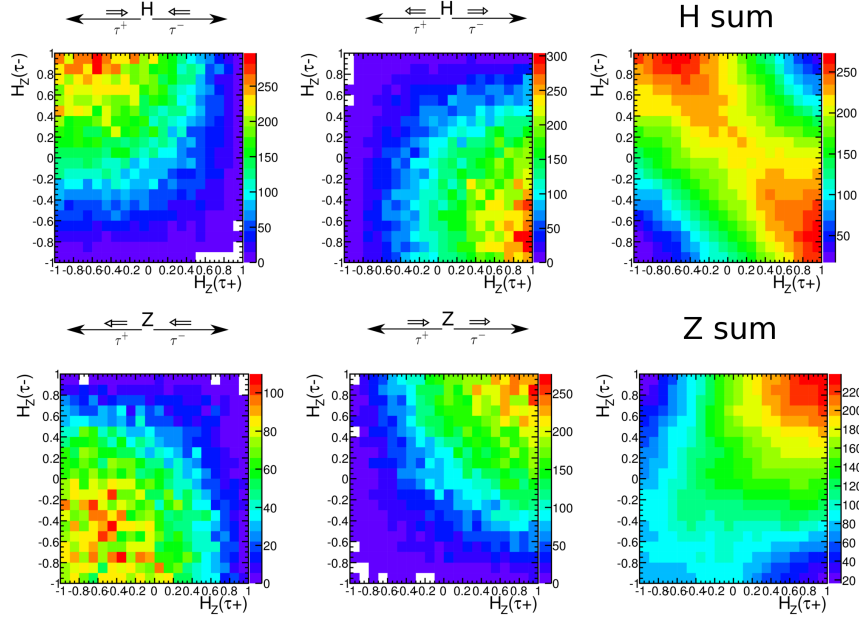


Figure A.2: Correlation between the polarimetric vectors on truth level divided in helicity combinations and total. $l\pi$ & $l\rho$ -channel. Please note that the color scheme is adjusted to the number of events in the respective plot.

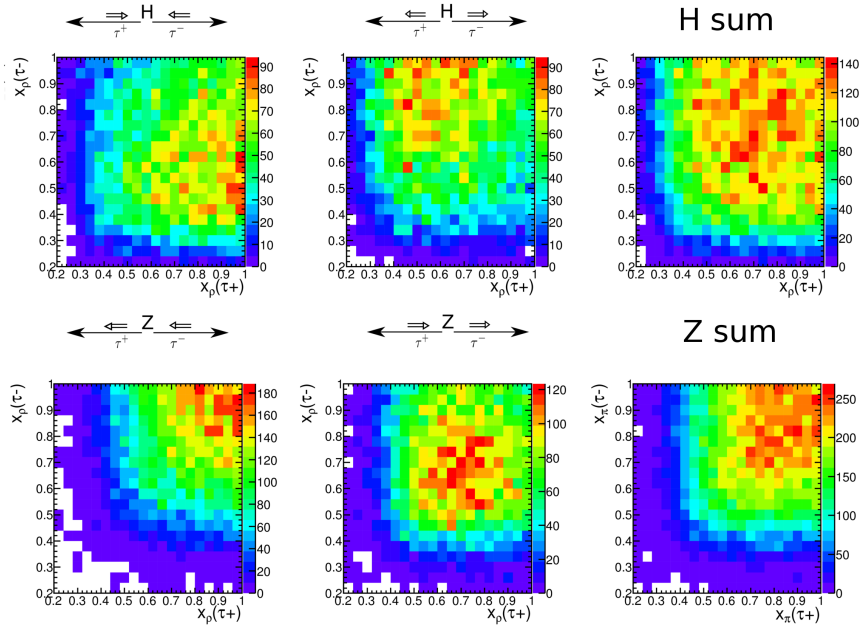


Figure A.3: Correlation between x_{τ} s on truth level divided in helicity combinations and total. $\rho\rho$ -channel. Please note that the color scheme is adjusted to the number of events in the respective plot. (cluster-based π^0 , MMC)

A.4 TMVA analysis in the $\rho\rho$ -channel

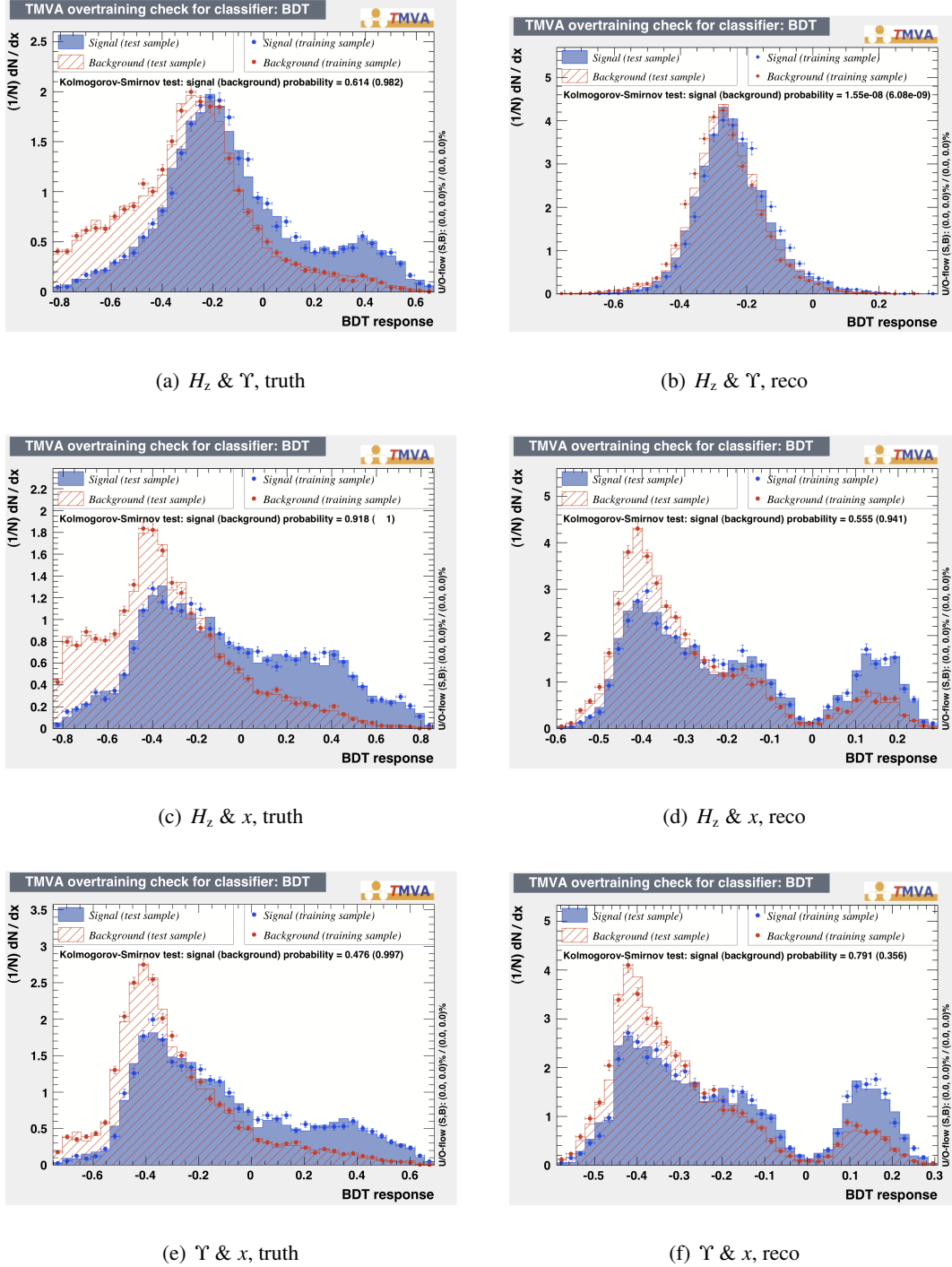


Figure A.4: BDT response calculated by TMVA for a combination of observables in the $\rho\rho$ channel.

Bibliography

- [1] P. W. Higgs. Broken symmetries, massless particles and gauge fields. *physics letters*, 12:132–133, 1964.
- [2] G. Aad et al. Observation of a new particle in the search for the Standard Model Higgs boson with the ATLAS detector at the LHC. *Phys.Lett.*, B716:1–29, 2012.
- [3] S. Chatrchyan et al. Observation of a new boson at a mass of 125 GeV with the CMS experiment at the LHC. *Phys.Lett.*, B716:30–61, 2012.
- [4] Search for the Standard Model Higgs boson in H- \rightarrow tau tau decays in proton-proton collisions with the ATLAS detector. Technical Report ATLAS-CONF-2012-160, CERN, Geneva, Nov 2012.
- [5] J. Beringer et al. Particle physics booklet, 2012.
- [6] I. Aitchison and A. Hey. *Gauge Theories in Particle Physics - A Practical Introduction*, volume 1. Institute of Physics Publishing, Bristol and Philadelphia, 2000.
- [7] National Aeronautics and Space Administration. Wmap news. <http://map.gsfc.nasa.gov/news/>.
- [8] S. P. Martin. A Supersymmetry primer. 1997.
- [9] Atlas detector and physics performance: Technical design report, 1. Technical report, Geneva, 1999.
- [10] Atlas photos. <http://www.atlas.ch/photos/full-detector-cgi.html>.
- [11] B. Resende vaz de Melo Xavier. Muon identification algorithms in atlas. European Physical Society Europhysics Conference on High Energy Physics EPS-HEP 2009, July 2009.
- [12] ATLAS Collaboration. Expected electron performance in the atlas experiment. Technical Report ATL-PHYS-PUB-2011-006, CERN, Geneva, Apr 2011.
- [13] M. Cacciari, G. P. Salam, and G. Soyez. The Anti-k(t) jet clustering algorithm. *JHEP*, 0804:063, 2008.
- [14] F. Friedrich. Tau Lepton Reconstruction and Identification at ATLAS. 2012.
- [15] B. Andersson et al. Parton fragmentation and string dynamics. Technical report.
- [16] T. Sjostrand, S. Mrenna, and P. Z. Skands. A Brief Introduction to PYTHIA 8.1. *Comput.Phys.Commun.*, 178:852–867, 2008.

- [17] S. Alioli et al. The powheg box. <http://powhegbox.mib.infn.it/>.
- [18] N. Davidson, T. Przedzinski, and Z. Was. Photos interface in c++. Technical Report CERN-PH-TH/2010-261, IFJPAN-IV-2010-6, CERN, Nov 2010.
- [19] S. Jadach, J. H. Kühn, and Z. Was. Tauola- a library of monte carlo programs to simulate decays of polarized τ leptons. *Computer Physics Communications*, 64(2):275 – 299, 1991.
- [20] Z. Was. TAUOLA the library for tau lepton decay, and KKMC / KORALB / KORALZ /... status report. *Nucl.Phys.Proc.Suppl.*, 98:96–102, 2001.
- [21] S. Agostinelli et al. Geant4—a simulation toolkit. *Nuclear Instruments and Methods in Physics Research Section A: Accelerators, Spectrometers, Detectors and Associated Equipment*, 506(3):250 – 303, 2003.
- [22] T. Åkesson et al. Atlas high-level trigger, data acquisition and controls technical design report. ATLAS Technical Design Reports ATLAS TDR-016, ATLAS Collaboration, 2003.
- [23] SM higgs production cross sections at $\sqrt{s} = 8$ TeV. <https://twiki.cern.ch/twiki/bin/view/LHCPhysics/CERNYellowReportPageAt8TeV>.
- [24] S. Heinemeyer et al. Handbook of LHC Higgs Cross Sections: 3. Higgs Properties. 2013.
- [25] A. Elagina et al. A new mass reconstruction technique for resonances decaying to $\alpha\tilde{N}\alpha\tilde{N}$. *Nuclear Instruments and Methods in Physics Research Section A: Accelerators, Spectrometers, Detectors and Associated Equipment*, 654(Issue 1):481–489, October 2011.
- [26] Z. Czynzula, T. Przedzinski, and Z. Was. TauSpinner Program for Studies on Spin Effect in tau Production at the LHC. *Eur.Phys.J.*, C72:1988, 2012.
- [27] T. Pierzchala et al. Spin effects in τ lepton pair production at lhc. *Acta Physica Polonica*, 32(4):1277, April 2001.
- [28] M. Trottier-Mcdonald. π^0 finder algorithm: Finding π^0 within τ decays. Talk at Missing Mass Calculator meeting at Cern, 17.10.2011.
- [29] B. Winter. Cell based reconstruction of π^0 s in hadronic τ decays. Talk at ATLAS Tau Workshop in Corfu, 10.04.2013.
- [30] M. Hodgkinson. eflowrec software in atlas. Talk at ATLAS Tau Workshop in Corfu, 10.04.2011.
- [31] A. Stahl. *Physics with Tau-Leptons*, volume 160 of *Springer Tracts in Modern Physics*. Springer, 2000.
- [32] B.K. Bullock, K. Hagiwara, and A.D. Martin. Tau polarization and its correlations as a probe of new physics. *Nuclear Physics B*, 395(3):499 – 533, 1993.
- [33] Z. Czynzula. *Search for New Physics in Tau-pair Events in Search for New Physics in Tau-pair Events in ATLAS at the LHC*. PhD thesis, University of Copenhagen, June 2009.
- [34] I. Deigaard. Measurement of the tau polarization in $z \rightarrow \tau\tau$ decays with the atlas detector. Master’s thesis, University of Copenhagen, May 2012.

- [35] A. Hoecker et al. *TMVA 4 Toolkit for Multivariate Data Analysis with ROOT*. CERN, tmva version 4.0.3 edition, November 2009.
- [36] P. Wagner. Proposal for a baseline substructure algorithm & plans towards release 19 reprocessing. One-day tau workshop at CERN, 23.07.2011.

List of Figures

2.1	Particles of the Standard Model (values from [5])	3
2.2	Higgs potential	6
3.1	schematic ATLAS detector [10]	9
3.2	Tracks of particles travelling through the ATLAS detector [10]	12
3.3	Schematic Proton-Proton Scattering Process	15
4.1	Cross-section and rates (luminosity $L = 1 \cdot 10^{34} \text{ cm}^{-2}\text{s}^{-1}$) for various processes in proton-(anti)proton collisions, as a function of the centre-of-mass energy [22].	17
4.2	Z boson production via quark anti-quark scattering.	18
4.3	Standard Model Higgs boson production cross sections at LHC at 8 TeV. The ggF and VBF processes are calculated in complex-pole-scheme, while other WH/ZH and ttH processes are calculated in zero-width-approximation [23].	19
4.4	Higgs production modes.	19
4.5	Standard Model Higgs boson decay branching ratios at 8 TeV [24].	20
4.6	mass distributions of the selected events in the Boosted category of the $H \rightarrow \tau_{\text{lep}}\tau_{\text{had}}$ channel for the 8 TeV analysis, estimated using the missing mass calculator (MMC) [25]. The selected events in data are shown together with the predicted Higgs boson signal $m_H = 125 \text{ GeV}$ stacked above the background contributions. For illustration only, the signal contributions have been scaled by a factor of 5. The last bin in the histograms contains the overflow. [4]	21
4.7	Correlation between τ helicities in the decaying boson rest frame for H/Z decaying into a pair of tau leptons. The thick arrows denote the helicities of the tau leptons.	21
5.1	Possible τ -decay modes.	23
5.2	Collinear Approximation	27
5.3	Neutrino p_T reconstructed with the MMC compared to its truth value.	29
5.4	Helicities assuming $m_\tau \rightarrow 0$ (denoted by double arrows) for a $\tau^- \rightarrow \pi^- \nu_\tau$ decay where the tau lepton is moving along the dashed line.	29
5.5	$x = \frac{E_\pi}{E_\tau}$ spectrum of pions from polarised tau leptons according to Equation 5.20.	30
5.6	Helicities (denoted by double arrows) for a $\tau^- \rightarrow \rho^- \nu_\tau$ decay where the tau lepton is moving along the dashed line with the production of a transversely polarized rho meson.	30
5.7	The angular decay distribution in the laboratory frame for the decay $\tau \rightarrow \rho \nu_\tau$ [33]	32
5.8	$x_l = \frac{E_l}{E_\tau}$ spectrum of leptons from polarised tau leptons according to Equation 5.30.	32
5.9	Decay $\rho^- \rightarrow \pi^- \pi^0$ where the ρ is moving along the dashed line.	33

5.10	The distribution of the charged energy asymmetry, from rho decays divided into left-handed (pink) and right-handed (blue) samples. Each sample is normalized to one [34].	33
5.11	Helicity dependence of lepton neutrino transverse energy compared to the total transverse neutrino energy in leptonic tau decays	34
6.1	Schematic view of a decision tree [35].	38
6.2	Fraction of visible energy for $\tau \rightarrow \nu_\tau \pi$ decays (truth information).	39
6.3	Performance of different reconstruction methods for fraction of visible energy, $\tau \rightarrow \nu_\tau \pi$ decays split into tau polarisation.	40
6.4	Performance of different reconstruction methods for fraction of visible energy, $\tau \rightarrow \nu_\tau \bar{\nu}_l l$ decays split into polarisation.	41
6.5	Performance of different reconstruction methods for the charged energy asymmetry in $\tau \rightarrow \nu_\tau \rho$ decays.	42
6.6	Event-by-event difference between true and reconstructed Υ for truth matched $\tau \rightarrow \rho \nu_\tau$ events.	43
6.7	Polarimetric vector H_z correlation on truth level with fraction of visible energy x in $\tau \rightarrow \nu_\tau \pi$ decays	44
6.8	Polarimetric vector H_z correlation on truth level with other polarisation observables in $\tau \rightarrow \nu_\tau \rho$ decays	44
6.9	Polarimetric vector H_z reconstruction effects split into reconstructed (cluster-based π^0) and true number of neutral pions (1 π^\pm on truth level) respectively. For each of the coloured histograms only one particle type is reconstructed. This is either the neutrino using the MMC, the neutral pion using the cluster-based algorithm or the track(s). The black histogram gives the true distribution.	46
6.10	Polarimetric vector H_z reconstruction in the reconstructed single pion and rho channel. For each of the coloured histograms only one particle type is reconstructed, this is either the neutrino using the MMC, the neutral pion using the cluster-based algorithm or the track(s). The black histogram gives the true distribution and the dashed histogram the total reconstruction.	47
6.11	Correlation between the fractions of visible energy on truth level divided in helicity combinations and total. $\pi\pi$ -channel. Please note that the color scheme is adjusted to the number of events in the respective plot.	49
6.12	Correlation between Υ 's on truth level divided in helicity combinations and total. $\rho\rho$ -channel. Please note that the color scheme is adjusted to the number of events in the respective plot.	49
6.13	Correlation between the polarimetric vectors on truth level divided in helicity combinations and total. $\rho\rho$ -channel. Please note that the color scheme is adjusted to the number of events in the respective plot.	50
6.14	Correlation between x_τ on reconstruction level divided in helicity combinations and total. $\pi\pi$ -channel. Please note that the color scheme is adjusted to the number of events in the respective plot. (cluster-based π^0 , MMC)	51
6.15	Correlation between Υ 's on reconstruction level divided in helicity combinations and total. $\rho\rho$ -channel. Please note that the color scheme is adjusted to the number of events in the respective plot. (cluster-based π^0)	52

6.16	Correlation between H_Z s on reconstruction level divided in helicity combinations and total. $\rho\rho$ -channel. Please note that the color scheme is adjusted to the number of events in the respective plot. (cluster-based π^0 , MMC)	52
6.17	Correlation between x_ρ on reconstruction level divided in helicity combinations and total. $\rho\rho$ -channel. Please note that the color scheme is adjusted to the number of events in the respective plot. (cluster-based π^0 , MMC)	53
6.18	BDT response calculated by TMVA for the combination of all observables in the $\rho\rho$ channel.	54
A.1	Performance of different reconstruction methods for charged energy asymmetry, $\tau \rightarrow \nu_\tau\rho$ decays split into polarisation for truth matched channel.	58
A.2	Correlation between the polarimetric vectors on truth level divided in helicity combinations and total. $l\pi$ & $l\rho$ -channel. Please note that the color scheme is adjusted to the number of events in the respective plot.	59
A.3	Correlation between $x_{\pi s}$ on truth level divided in helicity combinations and total. $\rho\rho$ -channel. Please note that the color scheme is adjusted to the number of events in the respective plot. (cluster-based π^0 , MMC)	59
A.4	BDT response calculated by TMVA for a combination of observables in the $\rho\rho$ channel.	60

List of Tables

2.1	Multiplet-structure of fermions in the Standard Model.	5
4.1	Branching fractions for Z boson decays taken from [5].	18
5.1	τ -lepton branching fractions taken from [5]. " h^\pm " stands for π^\pm or K^\pm	24
5.2	Probability for the configuration of longitudinal polarisation of the tau leptons from different origins [27]. The probability of the helicity states $p_{\tau Z}$ is a function of the scattering angle and the center-of-mass squared of the hard process.	24
6.1	Monte Carlo samples used for the analysis. The Z boson sample is an official ATLAS sample revised with additional cell-based and efowRec π^0 reconstruction information	35
6.2	Cut criteria for particle selection	36
6.3	Additional channel specific requirements	36
6.4	Estimators of the separation power of different x_π calculation methods	41
6.5	Estimators of the separation power of different x_l calculation methods	41
6.6	Estimators of the separation power of different Υ calculation methods	43
6.7	Truth-reconstruction difference standard deviation for polarimetric vector H_z . Only one particle type is reconstructed at the same time, this is either the neutrino using the MMC, the neutral pion using the cluster-based algorithm or the track(s).	45
6.8	Separation of H_z on truth and reconstruction level	45
6.9	H/Z -distinction power for different observables on truth level	48
6.10	H/Z -distinction power for different observables on reconstruction level	53
6.11	H/Z -distinction power for combination of observables calculated by TMVA for BDT method. The error on the separation and the significance due to the TMVA settings is tested to be in the order of 0.002	54
A.1	Covered pseudorapidity regions of the Inner Detector taken from [9].	57
A.2	Covered pseudorapidity regions of the Calorimeters taken from [9].	57
A.3	Covered pseudorapidity regions of the muon spectrometer taken from [9].	57

